

# NAVAL POSTGRADUATE SCHOOL MONTEREY, CALIFORNIA



## THESIS

### BORO-SILICATE POLYCAPILLARY LENS FOR COLLIMATION OF X-RAYS

by

Michael B. Chase

June, 1997

Thesis Advisor:

Xavier K. Maruyama

Approved for public release; distribution is unlimited.

DTIC QUALITY INSPECTED 3

19980113 024

REPORT DOCUMENTATION PAGE			Form Approved OMB No. 0704-0188	
Public reporting burden for this collection of information is estimated to average 1 hour per response, including the time for reviewing instruction, searching existing data sources, gathering and maintaining the data needed, and completing and reviewing the collection of information. Send comments regarding this burden estimate or any other aspect of this collection of information, including suggestions for reducing this burden, to Washington Headquarters Services, Directorate for Information Operations and Reports, 1215 Jefferson Davis Highway, Suite 1204, Arlington, VA 22202-4302, and to the Office of Management and Budget, Paperwork Reduction Project (0704-0188) Washington DC 20503.				
1. AGENCY USE ONLY (Leave blank)		2. REPORT DATE June, 1997		3. REPORT TYPE AND DATES COVERED Master's Thesis
4. TITLE AND SUBTITLE BORO-SILICAT POLYCAPILLARY LENS FOR COLLIMATION OF X-RAYS			5. FUNDING NUMBERS	
6. AUTHOR(S) Michael B. Chase				
7. PERFORMING ORGANIZATION NAME(S) AND ADDRESS(ES) Naval Postgraduate School Monterey CA 93943-5000			8. PERFORMING ORGANIZATION REPORT NUMBER	
9. SPONSORING/MONITORING AGENCY NAME(S) AND ADDRESS(ES)			10. SPONSORING/MONITORING AGENCY REPORT NUMBER	
11. SUPPLEMENTARY NOTES The views expressed in this thesis are those of the author and do not reflect the official policy or position of the Department of Defense or the U.S. Government.				
12a. DISTRIBUTION/AVAILABILITY STATEMENT Approved for public release; distribution is unlimited.			12b. DISTRIBUTION CODE	
13. ABSTRACT (maximum 200 words) <p>The purpose of this thesis is to investigate the collimation of x-rays produced by transition radiation using the NPS Electron Linear Accelerator. These measurements support the theory that x-rays can be focused using a boro-silicate array of polycapillaries consisting of 258 bundles with 1387 micro-channels each. A 90 MeV electron beam incident upon a non-resonant mylar stack formed transition radiation spatially distributed in an annular cone. The electron beam was deflected 30 degrees using a rare earth permanent magnet. The diverging x-rays incident upon the lens array were transported through total external reflection and directed out of the array onto a phosphor screen. A digital camera recorded the phosphorescing image of the screen. Pixel intensity was analyzed to determine x-ray intensity as a function of two dimensional spatial distribution.</p> <p>Column average profiles of the pixel intensity show that the transition radiation intensity retains its Gaussian distribution after being redirected from a diverging beam into a mostly parallel beam. The intensity of the x-rays decreased by a factor of 0.72 due to the obstructed area at the face of the array and to imperfect admittance of the diverging x-ray cone into the polycapillary array.</p>				
14. SUBJECT TERMS X-Ray focusing, Transition Radiation, Linear Accelerator, X-Ray Lithography, polycapillaries			15. NUMBER OF PAGES 90	
			16. PRICE CODE	
17. SECURITY CLASSIFICATION OF REPORT Unclassified	18. SECURITY CLASSIFICATION OF THIS PAGE Unclassified	19. SECURITY CLASSIFICATION OF ABSTRACT Unclassified	20. LIMITATION OF ABSTRACT UL	

NSN 7540-01-280-5500

Standard Form 298 (Rev. 2-89)  
Prescribed by ANSI Std. Z39-18 298-102



Approved for public release; distribution is unlimited.

**BORO-SILICATE POLYCAPILLARY LENS FOR COLLIMATION OF X-RAYS**

Michael B. Chase  
Lieutenant Commander, United States Navy  
B.A., The College of William and Mary in Virginia, 1979  
M.B.A., Jacksonville University, 1988

Submitted in partial fulfillment of the  
requirements for the degrees of

**MASTER OF SCIENCE IN APPLIED PHYSICS**

from the

**NAVAL POSTGRADUATE SCHOOL**

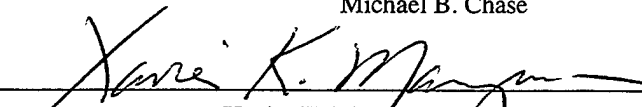
**June, 1997**

Author:

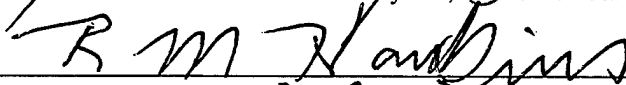


Michael B. Chase

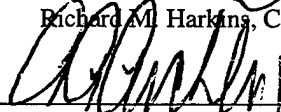
Approved by:



Xavier K. Maruyama, Thesis Advisor



Richard M. Harkins, Co-Advisor



Anthony A. Atchley, Chair  
Department of Physics



## ABSTRACT

The purpose of this thesis is to investigate the collimation of x-rays produced by transition radiation using the NPS Electron Linear Accelerator. These measurements support the theory that x-rays can be focused using a boro-silicate array of polycapillaries consisting of 258 bundles with 1387 micro-channels each. A 90 MeV electron beam incident upon a non-resonant mylar stack formed transition radiation spatially distributed in an annular cone. The electron beam was deflected 30 degrees using a rare earth permanent magnet. The diverging x-rays incident upon the lens array were transported through total external reflection and directed out of the array onto a phosphor screen. A digital camera recorded the phosphorescing image of the screen. Pixel intensity was analyzed to determine x-ray intensity as a function of two dimensional spatial distribution.

Column average profiles of the pixel intensity show that the transition radiation intensity retains its Gaussian distribution after being redirected from a diverging beam into a mostly parallel beam. The intensity of the x-rays decreased by a factor of 0.72 due to the obstructed area at the face of the array and to imperfect admittance of the diverging x-ray cone into the polycapillary array.



## TABLE OF CONTENTS

I. INTRODUCTION .....	1
A. THE NEED FOR X-RAY FOCUSING .....	1
B. THE USE OF TRANSITION RADIATION AS AN X-RAY SOURCE .....	2
C. POLYCAPILLARY LENS USE FOR X-RAY FOCUSING .....	5
D. PARABOLIC MIRROR FOR X-RAY FOCUSING .....	10
II. EXPERIMENTAL APPARATUS AND PROCEDURE .....	13
A. TRANSITION RADIATION STACK .....	13
B. THE POLYCAPILLARY LENS ARRAY .....	14
C. LENS ARRAY COMPONENTS .....	15
D. THE PHOSPHOR SCREEN .....	19
E. X-RAY IMAGING .....	19
F. PARABOLIC MIRROR FOR X-RAY FOCUSING .....	22
III. OBSERVATIONS AND DATA ANALYSIS .....	25
A. POLYCAPILLARY LENS DATA ANALYSIS .....	25
B. PARABOLIC MIRROR DATA ANALYSIS .....	29
IV. CONCLUSIONS .....	37
APPENDIX A. THE THEORIES AND THE PHYSICS .....	39
A. CHRENKOV VERSUS TRANSITION RADIATION .....	39
B. TRANSITION RADIATION THEORY .....	42
C. SNELL'S LAW OF REFLECTION AND REFRACTION .....	45
D. POLYCAPILLARY WAVEGUIDE OPTICS .....	49
APPENDIX B. LITHOGRAPHY APPLICATIONS .....	53
A. POLYCAPILLARY LENS USE IN X-RAY LITHOGRAPHY .....	53
B. THE STEPS IN THE LITHOGRAPHIC PROCESS .....	54
C. X-RAY LITHOGRAPHY .....	55
APPENDIX C. THE NPS LINEAR ACCELERATOR .....	57
A. INTRODUCTION TO THE LINAC .....	57
B. THEORY OF ELECTRON LINEAR ACCELERATION .....	58
C. ELECTRON EMISSION .....	59
D. ELECTRON MOTION IN A UNIFORM ELECTRIC FIELD .....	60
E. RELATIVISTIC ELECTRON MASS INCREASE .....	61
F. ACCELERATING STRUCTURE .....	64
G. THE RF POWER SYSTEM .....	66
H. ELECTRON BEAM INJECTION .....	67
I. THE RESONANT CAVITY .....	69
J. THE KLYSTRON .....	72
K. THE DEFECTION SYSTEM .....	74
L. THE END-STATION TARGET CHAMBER .....	75



LIST OF REFERENCES .....	77
INITIAL DISTRIBUTION LIST .....	79

## ACKNOWLEDGEMENTS

The author would like to thank several people for their assistance provided during this thesis research. First I would like to thank Xavier Maruyama from the Naval Postgraduate School, my primary thesis advisor, for introducing me to the world of Nuclear Physics, for his inspiration, and for his guidance. I would like to thank Melvin Piestrup from Adelphi Technology Inc, for conceiving and sharing his work on x-ray focusing, which became the center of my own thesis research. I would like to thank Ira Klotzko from X-Ray Optical Systems, Inc, for sharing his ideas on glass polycapillaries and for providing the polycapillary lens used in my thesis research. I would like to thank Don Snyder and Harold Rietdyk from the Naval Postgraduate School, for assembling the experiment and operating the Naval Postgraduate School accelerator. And most of all I would like to thank my wife Deborah and our children Micah, Jacob, and Joshua for their encouragement and influence in allowing me to attain this goal.

## I. INTRODUCTION

### A. THE NEED FOR X-RAY FOCUSING

Semiconductor devices have propelled our society into the electronic age. Currently, manufacturing techniques depend mainly on optical lithography techniques for production. Optical lithography uses light to illuminate a photoresist layer by passing the light through a mask, which is an image of the desired circuit. As technology companies design faster, denser, and cheaper silicon devices, optical lithography will reach a limit on available resolution because of the blurring between minimum line separations on photoresist surfaces due to the diffraction properties of light.

Local divergence is caused by Fresnel diffraction of the x-ray radiation as it passes through the mask. Each edge of the mask experiences a knife edge diffraction pattern. X-rays are attenuated and phase shifted at the edge. Due to the incoherent radiation incident on the edge, the diffraction pattern has a blurred edge and not the familiar fringed boundary Fresnel pattern of alternating high and low intensity lines from a laser passing through a slit. Global divergence occurs because the x-rays diverge from a finite sized source. Any distance between the source and the wafer will exacerbate the divergence effects on the resist. This increasing of the angle of incidence of the x-rays as we move away from the normal position on the wafer creates larger features on the resist. (Klotzko, 1996)

The small wavelength of x-rays can provide better resolution than optical lithography, which equates to smaller features on semiconductor devices. For over ten years, scientists have struggled with various techniques to continue to improve the available resolution through manufacturing processes using electron beam, ion beam, or x-ray lithography. Semiconductor device manufacturers will not convert from optical to x-ray lithography until competition requires smaller wavelengths for higher line resolution. The technical challenges are currently being widely studied for this transition. The applications are diverse—x-ray microscopes, telescopes, detectors, and fabrication of micro-devices. A successful x-ray lithograph facility could produce the next generation of semiconductor devices—denser, faster, and eventually cheaper, perhaps.

## B. USE OF TRANSITION RADIATION AS AN X-RAY SOURCE

Soft x-rays have wavelengths 1000 times smaller than optical wavelengths, but they are difficult to generate and have properties that make them even more difficult to work with. When a charged particle transverses between two media of different dielectric constants, transition radiation occurs. A normal dipole radiation pattern is Lorentz boosted forward into a conical pattern with an annular shaped pattern impinging on the target. Emission intensity can be increased by stacking thin metal foils or mylar together with spacing between the layers of material. As an electron passes through the stack of foils which have been placed in a vacuum, it encounters sudden interfaces of different dielectric constants and radiates a cone of soft x-rays in the direction of travel.

Cherenkov radiation results when a charged particle moves through a dielectric medium faster than the phase velocity of light through that medium. The moving charged particle caused the medium along its track to be momentarily polarized thus generating a short electromagnetic pulse as it passes through each layer of material. The fields then propagate as radiation about the Cherenkov angle,  $\theta_c$ .

$$\cos\theta_c = \frac{c/n}{v}, \quad (1)$$

where  $c$  is the speed of light in a vacuum,  $n$  is the index of refraction of the medium, and  $v$  is the phase velocity of light in the medium. Cherenkov radiation takes the shape of a cone, or annulus in three dimensions. (Wartski, 1976)

Transition radiation occurs when a charged particle of constant speed passes through a boundary separating media of two different electromagnetic properties. When the boundary is abrupt, such as between a conductor and a dielectric, transition radiation is dependent on the trajectory of the particle and the intensity is strongly dependent on the energy of the particle. (O'Grady, 1986)

The total energy lost by transition radiation is proportional to the Lorentzian factor,  $\gamma_0$ .

$$\gamma = \left(1 - \frac{v^2}{c^2}\right)^{-1/2} = \frac{E}{mc^2} \quad (2)$$

where  $v/c$  is the ratio of the velocity of the electron to the speed of light in a vacuum,  $E$  is the electron's total energy, and  $mc^2$  is its rest energy. (Piestrup, 1992)

Normally, a particle does not radiate if the velocity is constant. Cherenkov radiation is produced when the velocity of a particle exceeds the phase velocity of light in that medium. The radiation occurs at the Cherenkov angle for an infinite medium, but for the finite length media, it is in fact a radiation pattern. (Maruyama, 1986)

When the medium is inhomogenous or when the particle passes through an interface between media of different permittivities, there is a resulting dipole moment that is not zero, regardless of the particle velocity. This is known as transition radiation. Transition radiation may be viewed as a special case of Cherenkov radiation because the index of refraction,  $n$ , is abruptly changed. Emission can be increased by adding multiple interfaces, either randomly as in a foam plastic, or periodically as in a stack of layered material. (Piestrup, 1992)

The minimum distance over which a charged particle and an electromagnetic wave can exchange energy is called the formation length. The formation length for a particular medium,  $i$ , is

$$z_i = \frac{2c}{\omega[1 - \frac{v}{c}(\epsilon_i - \sin^2 \theta)^{1/2}]} \quad (3)$$

where  $\epsilon_i = 1 - (\omega_i / \omega)^2$ ,  $\omega$  is the plasma frequency, and  $\theta$  is the angle of radiation emission.

Since the plasma frequency of a material is proportional to the square root of its density, and the cutoff frequency is proportional to the plasma frequency, it follows that the cutoff frequency is proportional to square root of the foil density (Votruba, 1991). Because the electrons are relativistic, Lorentz effects cause the x-ray pattern to be emitted into a cone in the direction of propagation. The spatial distribution from a random foil radiation pattern is in the form of an

annulus with peak x-ray emission occurring at  $\theta_{apex} \equiv \sqrt{1 - \frac{v}{c}}$ . The differential cross section for transition radiation production per photon-energy interval per solid angle may be expressed as a function of three factors:

$$\frac{d^2 N(\omega)}{d\omega d\Omega} = F_1 F_2 F_3, \quad (4)$$

where  $N(\omega)$  is the number of x-ray photons and  $\omega$  is frequency. The  $F_1$  factor is the contribution from a single interface and is given by:

$$F_1 = \frac{(1/137)\omega \sin^2 \theta}{16\pi^2 c^2} (z_1 - z_2)^2. \quad (5)$$

The  $F_2$  factor accounts for the coherent superposition of radiation from the two surfaces present on each foil. An optical analogy for  $F_2$  would be the constructive interference from a single slit diffraction experiment.

$$F_2 = 4 \sin^2 \frac{l_2}{z_2}, \quad (6)$$

where  $l_2$  is the foil thickness and  $z_2$  is the formation length in the medium. The formation lengths can be rewritten as

$$z_{1,2} = \frac{4\lambda}{\frac{1}{\gamma^2} + \frac{\omega_{p1,2}^2}{\omega^2} + \theta_r^2}. \quad (7)$$

where  $\omega_{p1,2}$  refers to the plasma frequency in the media. The  $F_3$  factor accounts for the contribution of the total number,  $N$ , of foils in the stack:

$$F_3 = \frac{\sin^2 N \left( \frac{l_1}{z_1} + \frac{l_2}{z_2} \right)}{\sin^2 \left( \frac{l_1}{z_1} + \frac{l_2}{z_2} \right)}. \quad (8)$$

If the foil stack is periodic, the maximum energy exchange occurs when the ratio of  $l_2$  to  $z_2$  is a half multiple of  $\pi$  and  $\frac{l_1}{z_1} + \frac{l_2}{z_2}$  is an integer multiple of  $\pi$ , such that :

$$\frac{d^2 N(\omega)}{d\omega d\Omega} = 4N^2 F_1. \quad (9)$$

(Piestrup, 1992)

### C. POLYCAPILLARY LENS USE FOR X-RAY FOCUSING

A method for focusing x-ray transition radiation was studied by M. A. Khumakhov of the Soviet Union in 1986. The theory of optical grazing incidence and total external reflection provides the foundation theory for his work. Light will perfectly reflect from a glass surface at a very shallow grazing angles. He proposed that multiple reflections of x-rays could take place on suitably curved optic surfaces. Provided the radius of curvature did not increase too much, glass capillaries could transport x-rays. Such a technique could effectively channel and focus x-rays!

This thesis will describe a series of experiments that took place from November 1996 through April 1997 at the Naval Postgraduate School 100 MeV Electron Linear Accelerator Facility. Because the linear accelerator requires vacuum pressures, at least 24 hours is needed between each modification in the chamber. The linear accelerator produced a 90 MeV electron beam at a current of about 35 nanoamperes, which was directed into the target chamber using magnetic deflection system.

Figure 1 shows the physical layout of the target chamber using the polycapillary lens. The electron beam from the linear accelerator is incident upon the mylar stack. The magnet bends the electron beam away from the longitudinal axis of the chamber so that the electrons will not damage the lens or interfere with the x-ray measurements. The transition radiation is in turn incident upon the polycapillary lens array. The x-rays are channeled through the polycapillaries and exit the lens where they impact the phosphor screen outside the longitudinal axis of the chamber. A Cohu solid state camera recorded the phosphor screen images for further analysis

using a Macintosh computer and a digital image analysis software program, *Image 1.3.2*. (Hollinger, 1989)

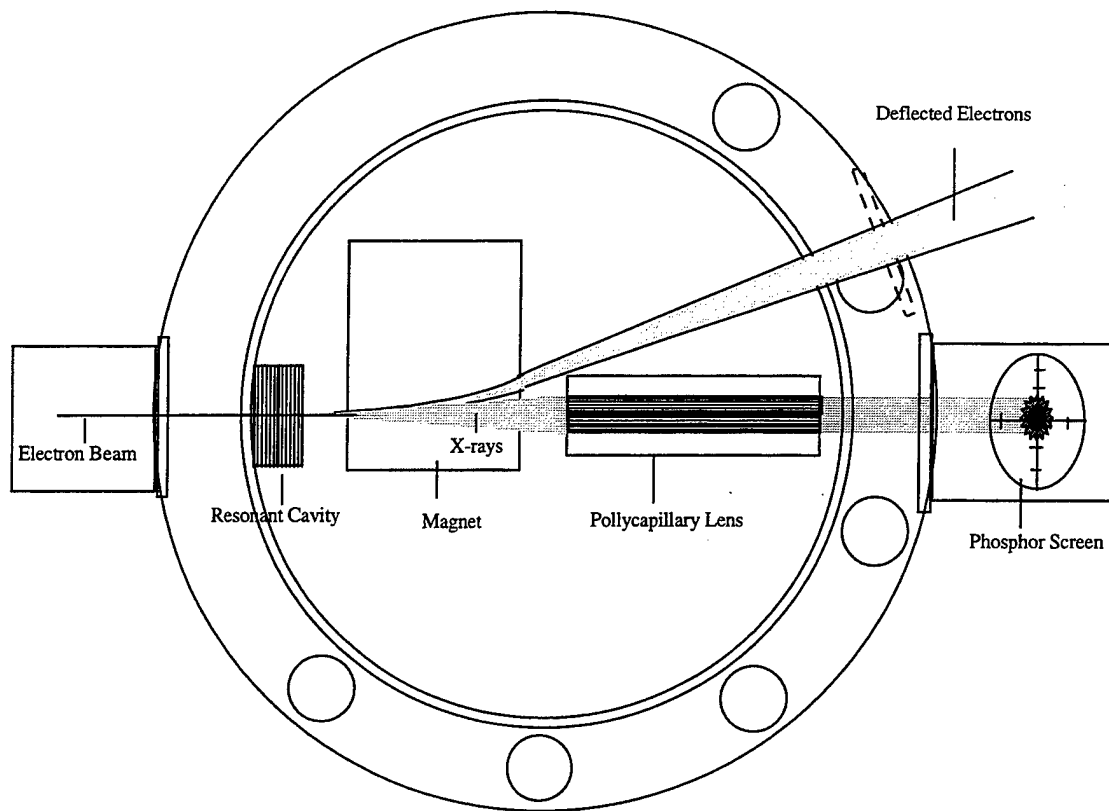


Figure 1. The target chamber layout during the experiment.

This first component inside the target chamber is the transition radiation stack, constructed by alternating layers of mylar foil with aluminum washers. Beryllium foil and grocery plastic wrap are also suitable for producing transition radiation. This produced transition radiation at soft x-ray energies. A large neodymium boron magnet with a rectangular groove was placed just after the stack. The electrons that pass through the stack and the x-rays generated in the stack both pass into the groove in the magnet. The electrons are deflected in the presence of a magnetic field and were diverted through the 30 degree port of the target chamber to a beam dump.



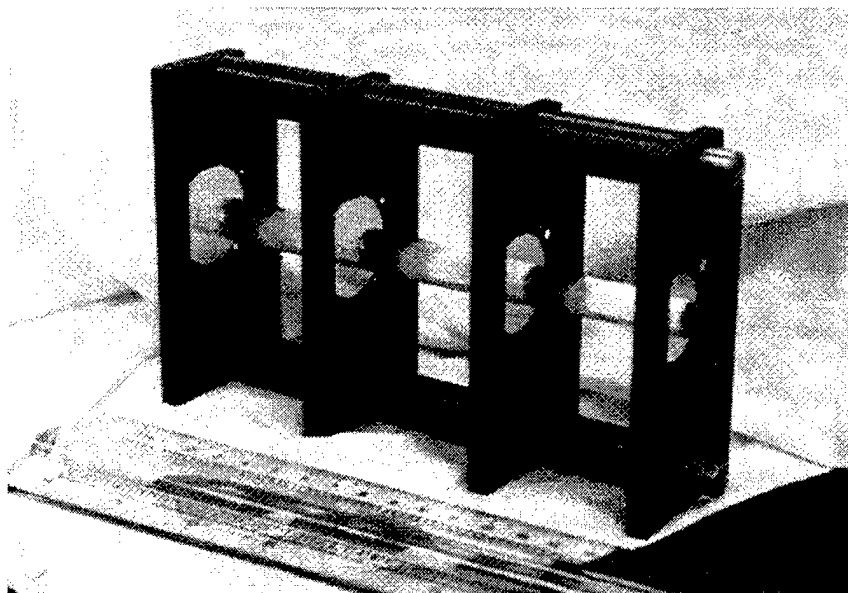


Figure 2. Polycapillary lens array.

The polycapillary lens array was constructed by X-Ray Optical Systems, Inc. It is designed in such a way that the opening part of the lens is made of small capillaries that are each parallel to the diverging x-rays. The capillaries then curve until they are all parallel so that the exit allows the x-rays to exit in a parallel fashion. This collimates a diverging source of x-rays into a parallel one that could be used in x-ray lithography. Diverging sources produce more distortions on surfaces than parallel sources. The x-rays passing through the lens array intercepted a phosphor screen that illuminated to indicate the shape and intensity of the x-ray beam. Figure 2 shows the polycapillary lens in its rigid holder.

The experiments conducted in this thesis consisted of analyzing and focusing this cone of x-rays produced by transition radiation. The diverging x-rays were first studied by letting them intercept a phosphor screen. X-rays cause the screen to phosphoresce. The screen was photographed using a CCD camera aligned with a glass covered opening. The digital file of the photograph was then analyzed using software to determine the intensity profile of the transition radiation before attempts were made to focus the x-rays. Figure 3 is an image of the x-ray illuminated phosphor screen.

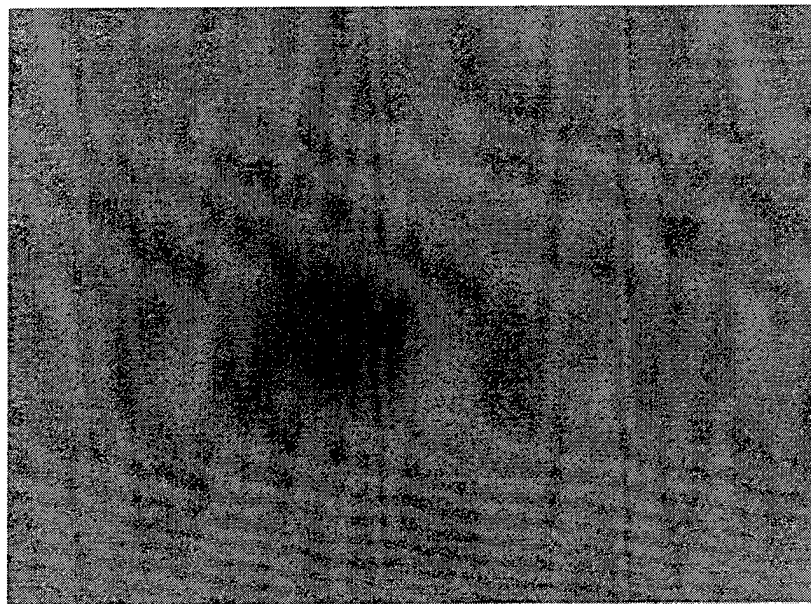


Figure 3. Phosphor screen illuminated with x-rays.

The polycapillary lens was then placed in the chamber so that the x-rays were incident on the entrance side on the lens. The exit side of the lens array pointed to the phosphor screen. Image analysis software was then used to determine the intensity characteristics of the x-ray beam exiting the lens.

Figure 4 below shows the relative intensities versus the horizontal position in mm of the image captured without the polycapillary lens in place as well as the plot of the image with the lens in place. The data comes from the column average analysis. The pixel intensity was derived by subtracting the background intensity and inverting the scale to give a positive intensity for the beam. The graph shows that while the general intensity distribution of the image is still Gaussian, the intensity has been reduced by a factor of 0.72.

Figure 5 is a polynomial curve fit of the intensity distributions of the images taken both with and without the lens in place normalized to have the same maximum peak. The full width half maximum of the image without the lens is 1.5 times that obtained with the lens in place. Figure 5 shows the lens effectively focuses the x-ray beam. Furthermore, despite the observed attenuation, the lens does not involve significant distortion.

### X-Ray Intensity as a Function of Horizontal Position

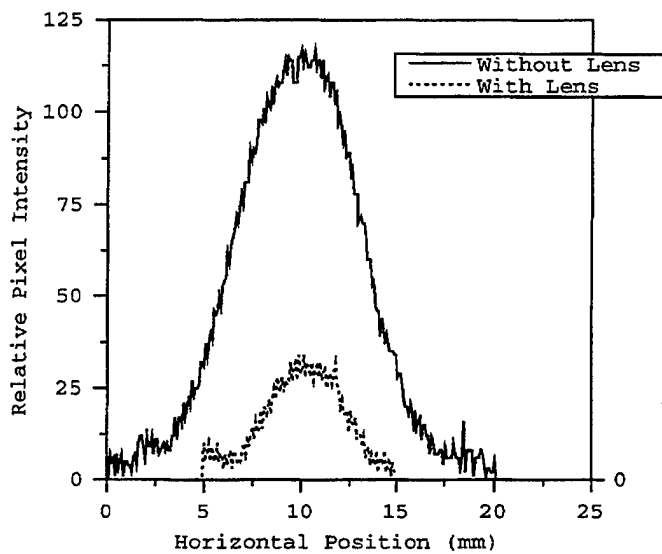


Figure 4. X-ray intensity comparison.

### Polynomial Curve Fit of Normalized Intensity Profiles

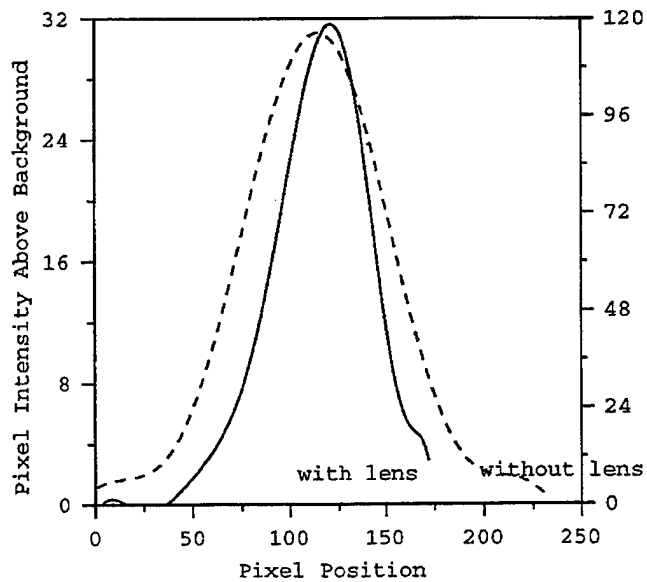


Figure 5. Half width intensity comparison.

#### D. PARABOLIC MIRROR FOR X-RAY FOCUSING

Following the experiments using the polycapillary, or Khumakov, lens, the chamber was modified to examine the reflecting capabilities of a single curved mirror. The mirror consisted of a 280 mm long strip of slightly tapered floated glass that had a thin layer of gold evaporated onto one surface. If the mirror were flat, then the reflected image would be circular because the transition radiation incident on the mirror produces a circular image, only it would be offset at twice the angle of reflection from the surface. However, the 11 mm wide lens was placed in a rocker that held the middle against its aluminum frame while the ends of the glass were bent using plastic screws. This gave the mirror a 10 meter radius of curvature. X-rays incident at grazing angles would now be reflected to produce an elliptical image, because they would be focused from a circular image into an elliptical shape. The exit port had to be modified with a tapered vacuum shim to accommodate a 3.3 degree offset.

Figure 6 shows the elliptical shape of the x-rays from the parabolic mirror.

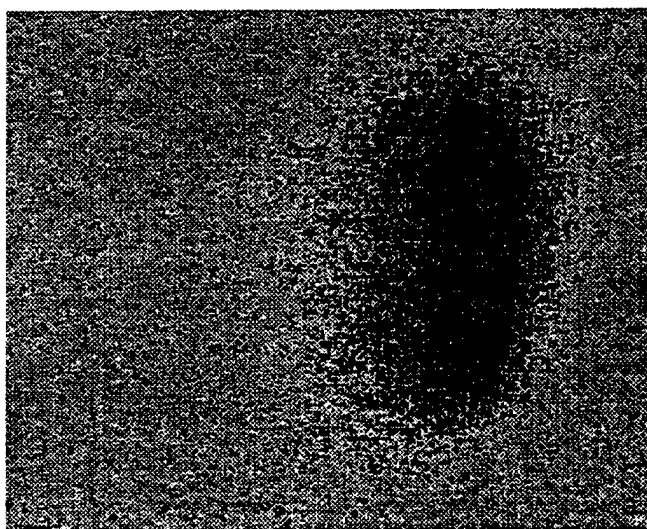


Figure 6. The image on the phosphor screen using the mirror lens

The analysis of the elliptical image showed that the highest intensity occurs in the central region and that it rapidly tapers off to background on the right side. The left side of the x-ray image was more "smeared" out, tapering off to background over a larger area. Figure 7 shows the plot of the x-ray intensity as a function of position. Additional experiments were performed

to determine if the elliptical image could be scanned across the phosphor screen. This would determine the suitability of using a scan technique to pass the x-rays across a mask to uniformly expose a mask. Figure 8 shows a schematic of this experiment. The mirror was rotated to six different positions and the x-ray image was photographed for analysis. Results indicate that the x-rays can be reflected across a fixed area. The intensity of the image was higher when the position on the screen was from the number 2 position until number 4 position (near the middle of the scan pattern). The area of the image increased towards the middle scan pattern compared to the edges of the fixed area. Overall, the intensity distribution was within a factor of two for positions 1 through 4.

Such a mirror could be rotated to scan x-rays in the lithograph process (Piestrup, 1997). This process is discussed in more detail later in this thesis.

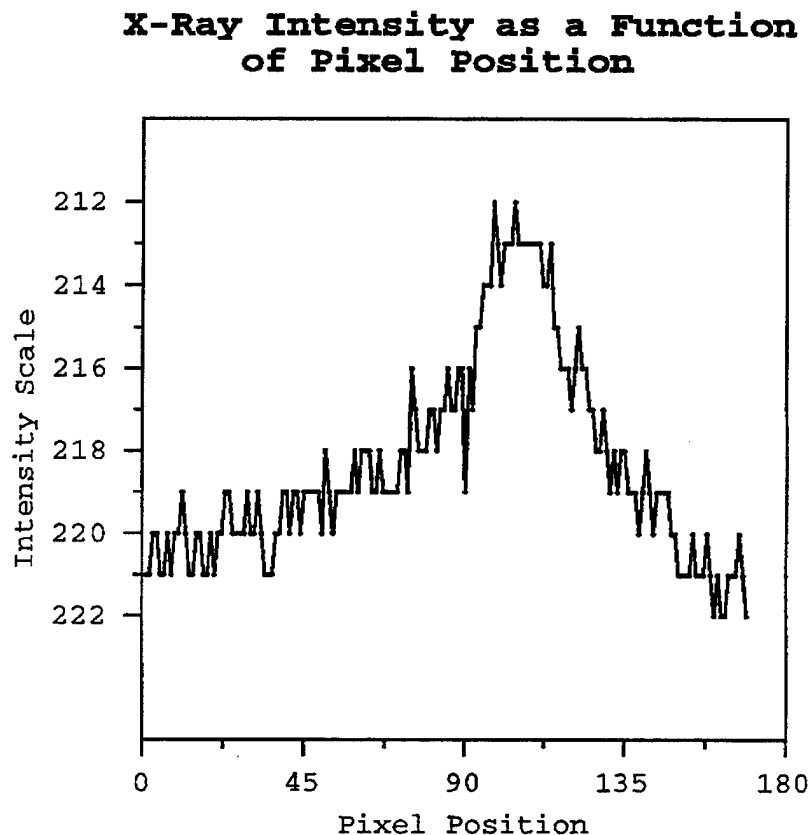


Figure 7. Spyglass graphics plot of pixel intensity distribution on mirror.

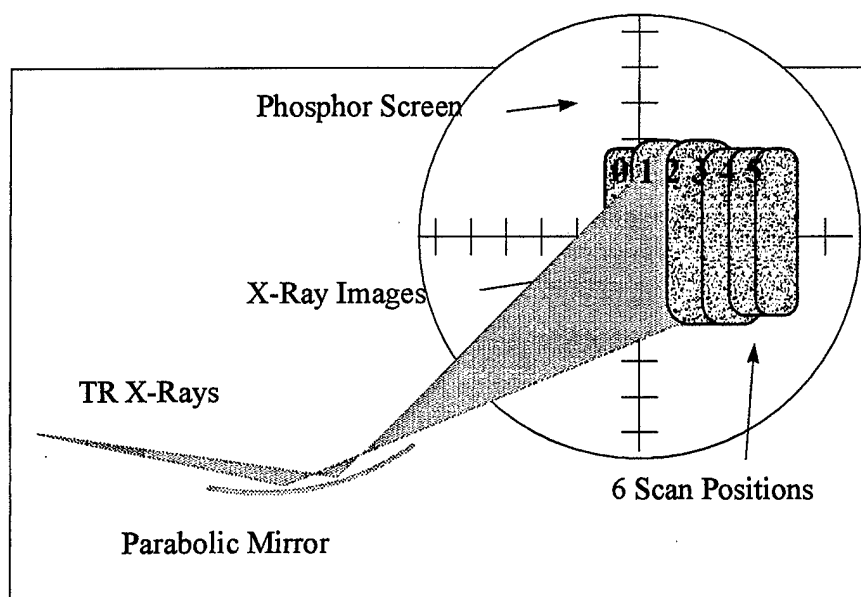


Figure 8. Scanning experiment schematic

## II. THE EXPERIMENTAL APPARATUS AND PROCEDURE

### A. TRANSITION RADIATION STACK

This first component inside the target chamber is the transition radiation stack. The stack consists of machined aluminum washers that alternate with squares of mylar plastic wrap. The mylar is taped flat to each washer. The washers are held together by long bolts placed in holes that have been drilled precisely along the sides of the washers. Several different stacks were used during the thesis experimentation, one with 23 layers, one with 41 layers, and one with 60 layers. beryllium foil and grocery plastic wrap are also suitable for producing transition radiation. A large neodymium boron magnet with a rectangular groove was placed just after the stack. The electrons that pass through the stack and the x-rays generated in the stack both pass into the groove in the magnet. The electrons are deflected in the presence of a magnetic field and were diverted through the 30 degree port of the target chamber to a dump. The electron beam will cause the clear mylar foils to darken and become brittle after several runs requiring a replacement stack. Figure 9 shows the diverging transition radiation pattern produced from the mylar stack.

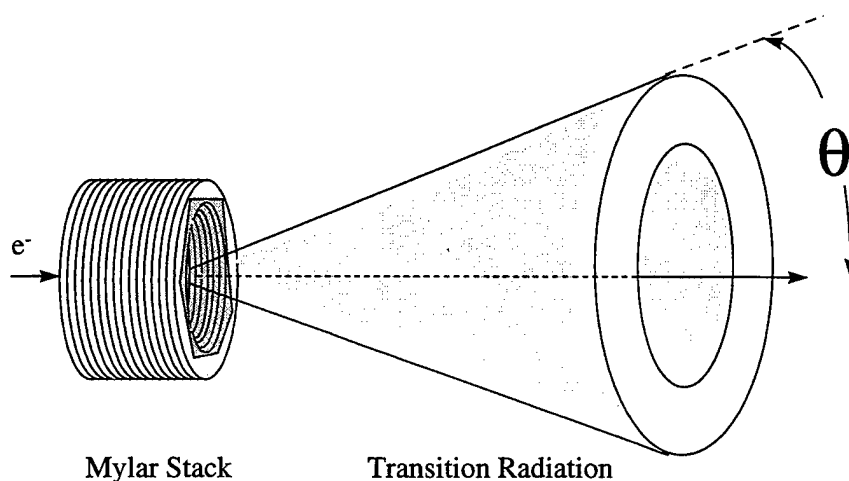


Figure 9. Transition radiation stack and radiation pattern.

Using a 41 layer mylar stack for production of transition radiation, the phosphor screen was set at the longitudinal exit port with the screen tilted 45 degrees and the camera positioned normal to the exit window. This provided a digital image as if the camera and beam were normal

to the screen. The digital camera recorded the phosphorescent image of the x-rays in the otherwise dark target chamber. The beam measured 1.2 cm in diameter for a beam current of one micro-ampere. The linac was then run without the lens in place. The neodymium boron magnet deflected the electrons and the x-rays incident upon the phosphor screen were photographed. A dozen images were recorded using *Image 1.3.2* software for analysis and comparison.

## B. THE POLYCAPILLARY LENS ARRAY

The polycapillary lens is an array of very small hollow glass tubes that reflect photons--electromagnetic energy in the form of light, or x-rays using total external reflection. The lens entrance geometry is conical shaped to tailor match the diverging source of x-rays from the transition radiation stack. The transition radiation exits in a diverging 10 milliradian cone. The array of small tubes is then gently bent to form a parallel geometry at the exit. The net effect is that the lens collimates a diverging source into a parallel source. Figure 10 shows the overall lens schematic from the central part of the lens bundle.

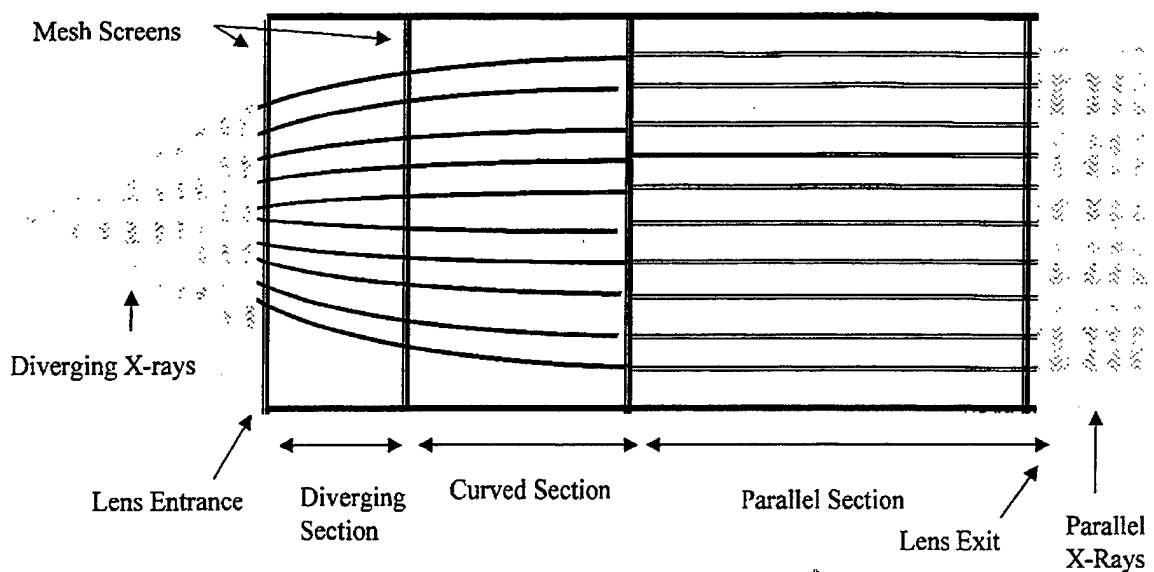


Figure 10. The overall schematic of a polycapillary lens array.

Transmission efficiency depends on the energy of the x-ray photons, the reflectivity of the surface of the glass medium, the vacuum in the external medium, the tube radius, the bending



radius, and the acceptance of x-rays at the polycapillary array entrance due to incident ray geometry (XOS, 1996). Under a National Science Foundation grant, X-Ray Optical Systems designed and built the polycapillary lens array for the experimental work performed in this thesis. This grant supported Dr. Melvin Piestrup and his associates at Adelphi, in studying x-ray focusing through the NSF Small Business Innovation Research program.

### C. LENS ARRAY COMPONENTS

The lens is an array of boron silicate glass capillaries. The details of the construction of the lens is proprietary information (XOS, 1996). Construction of such an array is possible by joining glass capillaries that have been heated and drawn down to form microcapillaries, which are then fused together into a hexagonal array of microcapillaries. This bundle is then gently heated and drawn down further to form a fiber optic sized micro-bundle. The micro-bundle, or polycapillary, is then carefully arranged in a mesh structure composed of parallel faces of specially formed metal to hold the polycapillaries in a predetermined geometry. The lens housing consists of a series of screens that hold the bundles in position to intercept the diverging x-rays and then curves the polycapillaries into a quasi-parallel array. Figure 11 shows a diagram of a mesh screen with a single bundle of polycapillaries fed into one opening. The completed array would have many such bundles. (Klotzko, 1996)

The lens used in this experiment consisted of an array of 258 polycapillaries that each contained 1387 individual channels with inside diameters of 8-50 microns. The fractional open area for such bundles can be as high as 65% (Klotzko, 1996). The optics have roughly circular input areas and are grouped into hexagonal shaped bundles that fit into the mesh screen. The individual polycapillaries are then grouped in a quasi-circular array using the mesh, an ultra-thin metal screen formed to hold the polycapillaries.

The original dimensions of the circular capillary is of the order of 5 cm diameter. These are drawn down to about 400 micrometer diameters and then fused together. The final diameter of the polycapillary is of the order of 10 microns diameter. There are 1387 channels in each of the 258 polycapillary bundles used in this experiment. In this experiment, the entrance face of the lens is oriented such that the individual polycapillary bundles are directed towards the diverging x-rays from the transition radiation sack. The 9 mm diameter array is roughly circular.

face of the lens is oriented such that the individual polycapillary bundles are directed towards the diverging x-rays from the transition radiation sack. The 9 mm diameter array is roughly circular. The polycapillary bundles are then channeled by the mesh screens into a parallel array. The 13 mm diameter exit face of the bundle is 150 mm from the entrance face. Figure 12 shows a photograph of the lens showing the entrance section of the lens. (Klotzko, 1996)

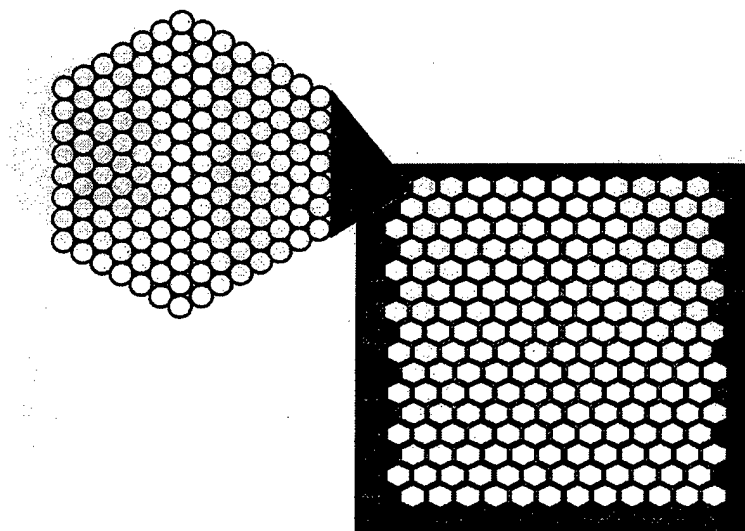


Figure 11. A bundle of polycapillaries in a single mesh screen opening.

Figure 13 is a scanning electron microscope photograph taken at the Naval Postgraduate School Scanning Electron Microscope Facility revealing the fine microstructure of a single polycapillary bundle. The diameter of the bundle is only 500 microns. Remarkably, the general shape of the original glass capillary is maintained throughout the drawing down process. The x-rays that are normally incident on the glass surface are attenuated in the glass medium. The x-rays that intercept the triangular open areas between the micro-capillaries are not effectively channeled due to the geometry of the inwardly rounded corners. The x-rays that enter the open area of the roughly circular openings will reflect at very shallow grazing angles inside the micro-channels. The diameter of the channels is 10 microns while the wavelength of the soft x-rays is between one angstrom to a nanometer. As the capillaries are curved, the reflection angle must

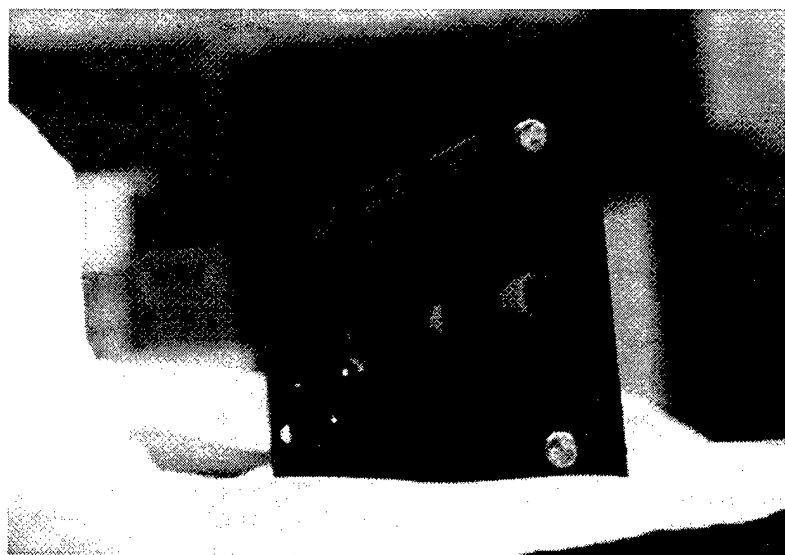


Figure 12. End view of Polycapillary lens array.

be below the critical angle for total external reflection to take place. The polycapillaries are waveguides for x-rays. The x-rays enter the channels axially or at very small angles due to the finite size of the source and due to the curving that takes place of the capillaries inside the lens array during collimation. The x-rays will exit the lens in a predominately parallel fashion, but will be slightly diverging due to the finite reflection angles that take place just before each x-ray photon departs the exit face. (Klotzko, 1996)

Figure 14 is a close-up of the same bundle showing the retained original shape of the polycapillary bundle. The final shape of the channel is between a circle and a hexagon. The inside surface roughness needs to be small compared to the wavelength of an x-ray, or the x-rays will be scattered inside the channel to angles equal to or greater than the critical angle. This would cause transmission losses inside the channel. The close-up reveals a tube diameter of only 10 microns and a glass thickness of approximately 1.5 microns.

The input of the lens was placed 250 mm from the transition radiation stack exit co-located inside the end station of the target chamber. This allowed the 10 milliradian diverging x-rays to expand to a 9 mm diameter circle incident upon the entrance face of the array. The phosphor screen was placed at the longitudinal exit of the target chamber.

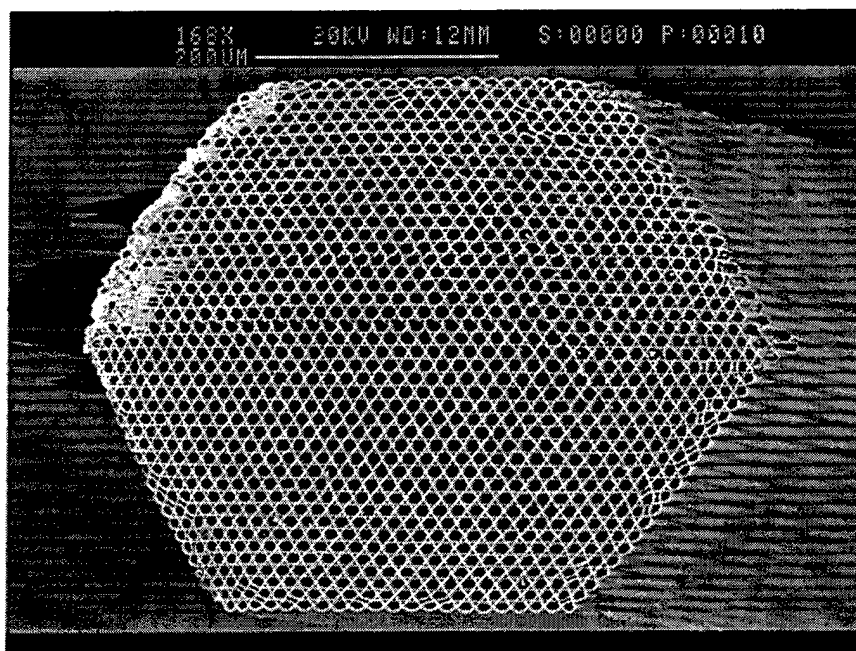


Figure 13. Scanning electron microscope photograph of a bundle.

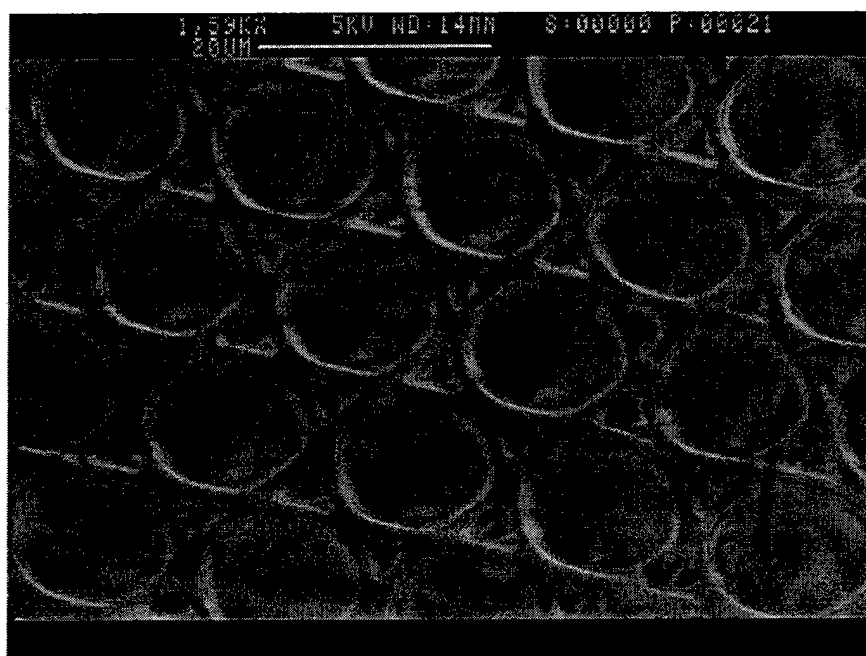


Figure 14. SEM close-up of polycapillary bundle.

#### D. THE PHOSPHOR SCREEN

The phosphor screen was mounted at 45 degrees to the beam and to the camera. The image was photographed using a solid state camera mounted directly above the screen. *Image 1.3.2* software was used to analyze the illuminated phosphor screen. Figure 3 showed the phosphor screen illuminated by the x-rays generated by the transition radiation stack without the lens in place. The electrons from the beams have been diverted with a neodymium boron magnet through the 30 degree port measured from the longitudinal axis of the primary exit port. The phosphor screen provides a qualitative measurement of relative x-ray intensity. A planar semiconductor or linear array of diodes might be used to specifically measure the intensities of x-rays used in the experiment.

#### E. X-RAY IMAGING

Figure 3 was a reverse color image of x-rays from the transition radiation stack without the lens in place taken by a solid state camera and captured using *Image 1.3.2* software. It shows the circular dark gray area on the phosphor screen. The incident x-rays cause the phosphor to glow, which is photographed using sensitive CCD cameras. Figure 15 shows the *Image 1.3.2* display of the column average taken from the run using no lens. The plot is taken from a 20.8 mm square segment from the image of the phosphor screen centered on the x-ray image. The x-ray produced a bright spot which is taken as a lower value by the software for display.

There were 240 vertical pixels used in the column average and the pixel intensity ran from 123 to 219 on a relative intensity scale of 0 to 250. The width of the plot is 190 pixels. Each pixel is 0.1 mm squared. The spatial distribution of the x-ray beam is Gaussian in intensity in a cylindrical system with the highest intensity in the center of the beam.

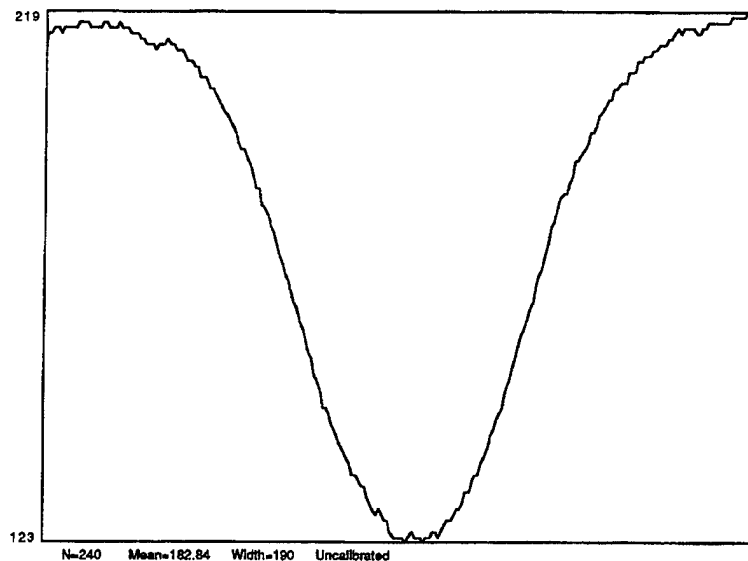


Figure 15. Image 1.3.2 display of column average plot for unfocused image.

Figure 16 is the Image 1.32 software analysis of the column average for the image of the pixel intensity distribution taken using the polycapillary lens. This is from a segment of the image 10.4 mm square with the x-ray image in the center. There were 104 bins used in the vertical image and 109 horizontally. The pixel intensity ran from 222 to 193, with the mean intensity measured of 207.6 on a relative scale of 0 to 250. The fractional fluctuation is higher on this image due to the smaller number of pixels averaged.

Histograms provide an indication of the uniformity of intensity distribution. The software provides 256 levels of pixel intensity from darkest background to highest measured intensity. A single line drawn on the image using the software could be analyzed to show which intensity bins were filled along the line. Histograms are not shown, but did provide the author a qualitative indication that the pixel intensity was uniform and not "spotty" inside the beam. The software also provides a time averaging function, but the speckle in the background tended to reduce the contrast between the x-rays and the background. The quality of the image also was rather dependent on the precise moment the picture was "snapped" and several pictures were examined before accepting a picture for analysis. A more rigorous (and time consuming...) analysis would average numerous profiles into a single composite graph.

The series of runs made with the 15 inch pipe extension between the target chamber and the phosphor screen determined if the x-rays exiting the lens were parallel. The diameter of the

image remained the same size, but greatly decreased in intensity by 72%. Figure 17 is a digital photograph of the image produced using the polycapillary lens array and the 15 inch extension. The lower quality of the electron beam that day may have contributed to the lower intensity or perhaps the camera was starting to fail. The sensitivity of cameras varied significantly. In theory, the intensity profile of the extended version should have been qualitatively identical with the short version with a slight increase due to the small divergence at each microcapillary. The deterioration of the images are suspected to be due to either radiation damage or oil vapor blockage of the capillary tubes, but this is only conjecture. Future experiments should further address this concern.

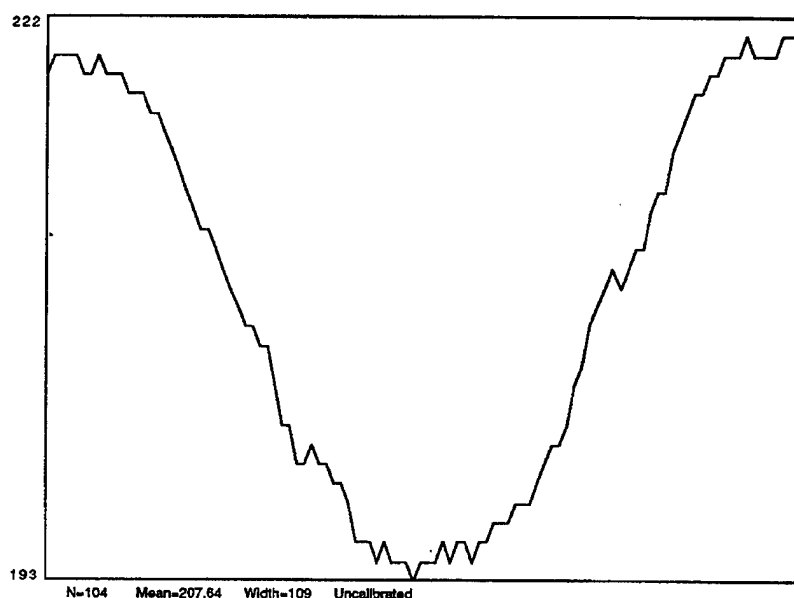


Figure 16. Column average of polycapillary lens focused image.

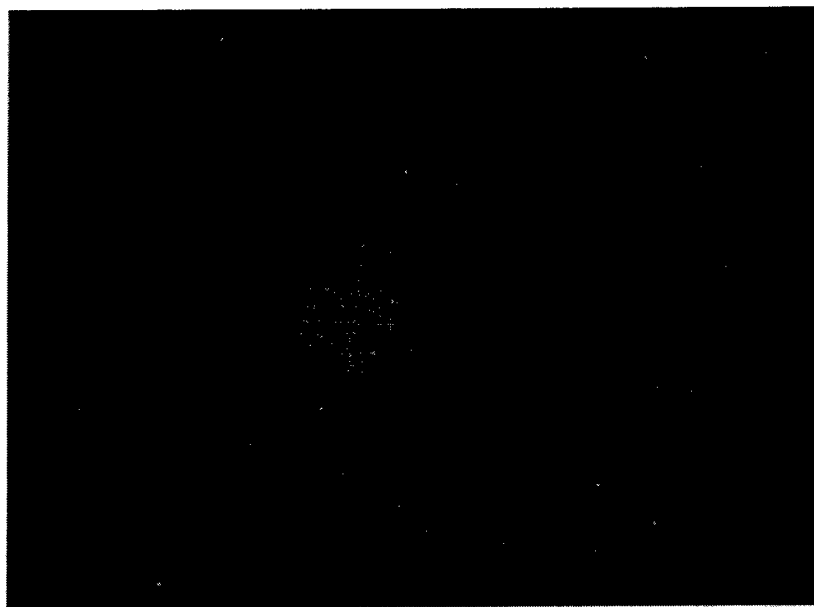


Figure 17. Digital image of x-rays focused on screen with 15 inch extension.

## F. PARABOLIC MIRROR FOR X-RAY FOCUSING

As an alternative to using the polycapillary lens array, a curved glass mirror was tested in the linac. The experimental setup was similar to the previous setup, except instead of using polycapillaries, a gold coated glass mirror was placed in the path of the incident x-rays. The mirror is a 287 mm x 10 mm (approximately 10" x 1/4") floated glass strip that has 600 Å of gold evaporated onto the surface to increase the reflectivity. Floated glass is produced by floating the liquid glass on a heavy liquid such that the surface is much smoother than rolled glass. The mirror is mounted on a 6 mm thick aluminum rocker that has screws to hold the mirror in place in the center and additional screws on the ends to bend the mirror into a parabolic shape. The mirror was bent to produce a 10 m radius of curvature and was placed in the incident beam at a 1.65 degree angle providing a 3.25 degree deflection from the longitudinal axis. An extension pipe was added to the target chamber exit to provide additional distance between the mirror and the phosphor screen. The target screen was located 650 mm from the mirror center. Figure 18 shows the new target chamber layout. (Piestrup, 1997)



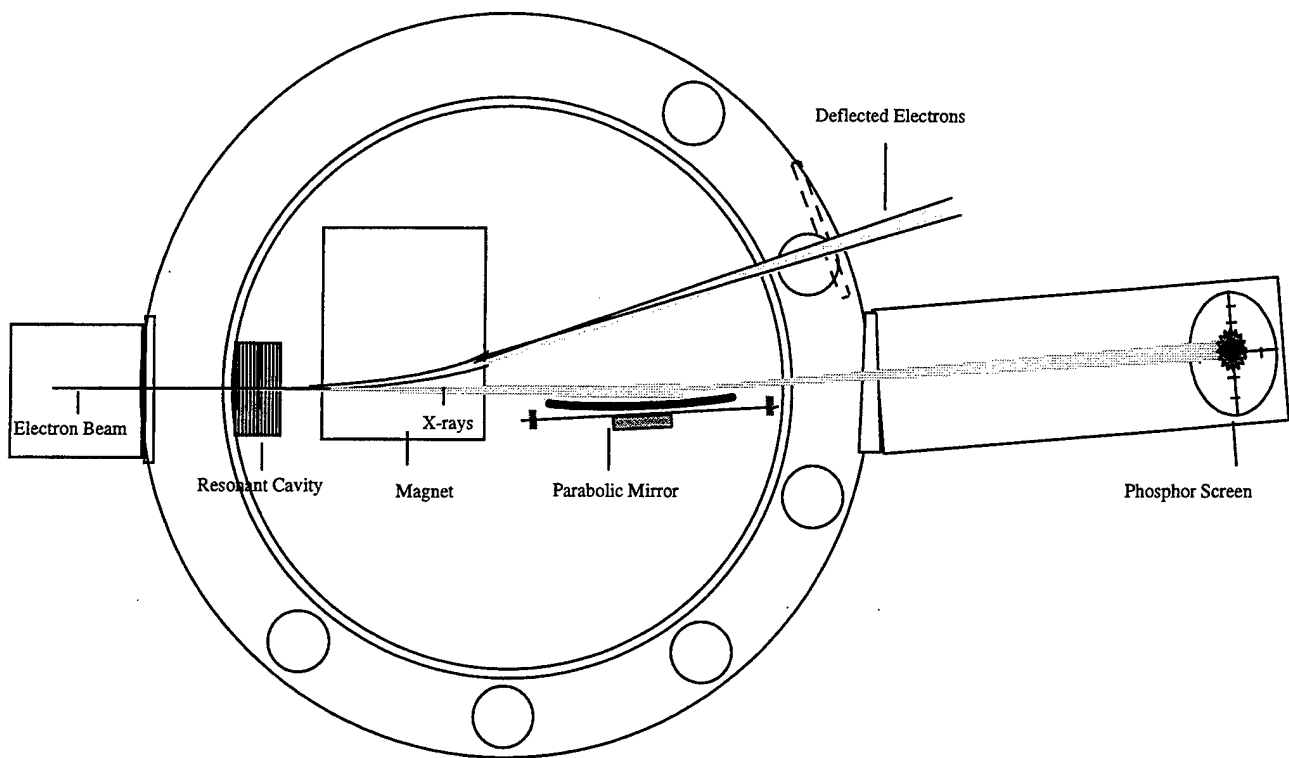


Figure 18. The experimental setup in the target chamber of the linac.

For a 20 milliradian divergent x-ray beam, a flat mirror produces an 18 mm circle on the screen. The 10 m radius of curvature should focus the circle down into an ellipse shape on the screen measuring 18 x 5 mm. The shape of the image can be changed by deforming the mirror. A parabolic mirror should produce an elliptical x-ray image. If the glass mirror were distorted in an additional dimension, the height of the image would also be reduced. The intensity of x-ray flux is increased per unit area due to the mirror curvature and can be adjusted by increasing or decreasing the curvature of the mirror. The screws holding the mirror could be attached to remotely controlled motors to change the image shape "real time."

Figure 19 shows a picture of the viewing port of the phosphor screen. The screen-camera arrangement remained the same as before to provide spatially stable photographs. X-ray images were then photographed and analyzed. The experiment produced an elliptically shape 15 x 5 mm image on the screen. Figure 6 was the *Image 1.3.2* capture of the x-rays reflected using the parabolic mirror onto the phosphor screen.

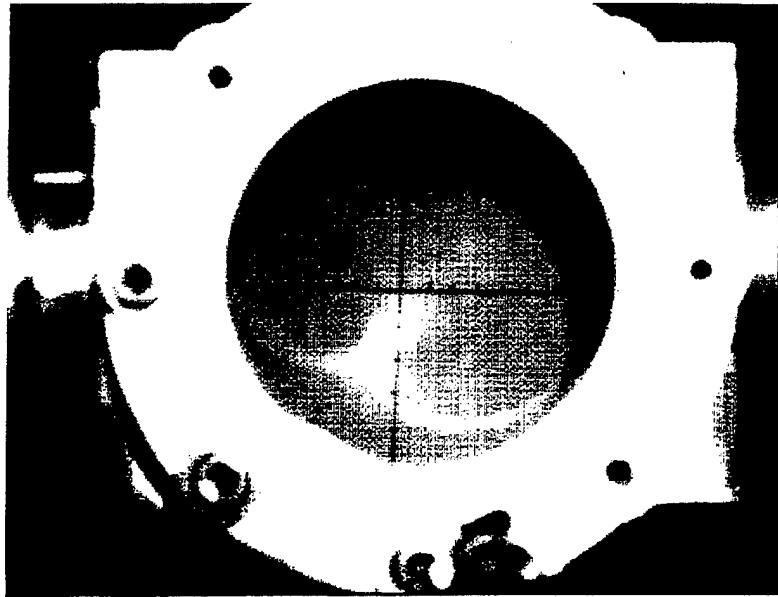


Figure 19. Phosphor screen port.

### III. OBSERVATIONS AND DATA ANALYSIS

#### A. POLYCAPILLARY LENS DATA ANALYSIS

This section will describe the materials used to capture the x-ray images and will discuss and analyze the data. The phosphor screen image was recorded using a CCD camera mounted above the screen at the end station. The screen was mounted at 45 degrees to the x-ray beam and in order to record geometrically correct images, the camera had to, in turn, be mounted at 45 degrees to the screen. The software used to analyze the x-ray image is called *Image 1.3.2*, a public domain program for the Macintosh II for digital image processing and analysis. *Image* can be used to acquire, display, and enhance images through histogram evaluation, contrast enhancement, density profiling, smoothing, sharpening, edge detection, and spatial convolution. *Image* is written using Think Pascal by the Symantec Corporation and was originally developed at the National Institutes of Health in Bethesda, MD (Hollinger, 1989). Most of the data analysis during this work was accomplished by making column average profiles of the intensity of the saved images from the phosphor screen. A more complete study of the x-rays would require expensive specialized instrumentation.

As discussed in the lens description earlier, the capillary collimating optics are designed to collect x-rays from a diverging source and collimate them into a parallel beam. The x-rays lose intensity because of the frontal area of the array that is blocked by the glass or by the triangular area between capillaries that does not effectively transport x-rays. Figure 20 shows the *Image 1.3.2* software control interface on a Macintosh II display in the NPS linac facility that were used in analyzing the data. There are newer software programs available on the open market for image processing and analysis, but the *Image 1.3.2* worked quite well for scrutinizing the phosphor screen images produced during these experiments.

This figure is a false color picture of the x-ray image using the lens. Contrast the size of the x-rays with the uncollimated picture in figure 3, the image without the lens in place. This is the *Image* software format page used in analyzing the transition radiation intensity. *Image* uses a function named *measure* to compute the area and mean density of the designated rectangular

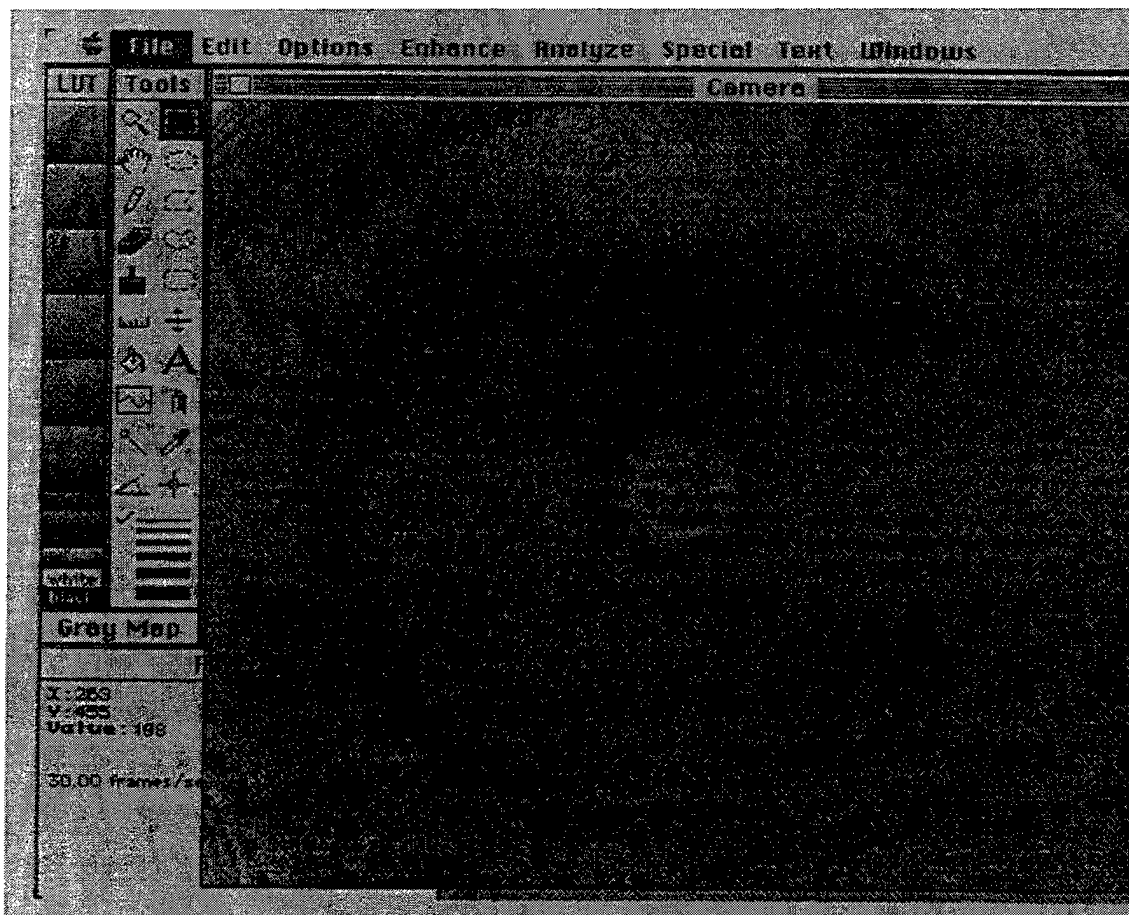


Figure 20. Image 1.3.2 Software Analysis display.

area on the screen. The image can be displayed in gray color or in a series of false color images. The contours present in the above image are based on the increasing intensity on the phosphor screen. The human eye is not able to discern the variation in a photograph image such as in Figure 3, but the pixel intensity is easily analyzed by software. Figure 21 is a column average plot, where the width of the plot is equal to the width of a selected 20.8 mm square section and each point represents the average intensity of the pixels in the corresponding column in the selection. This is a plot of the x-rays produced by the mylar stack after the electrons have been deflected away without the polycapillary lens in place. The overall distribution is Gaussian and indicates that the stack is not resonant. A cavity with appropriately spaced foils can produce resonant transition radiation which propagates in an annular intensity distribution.

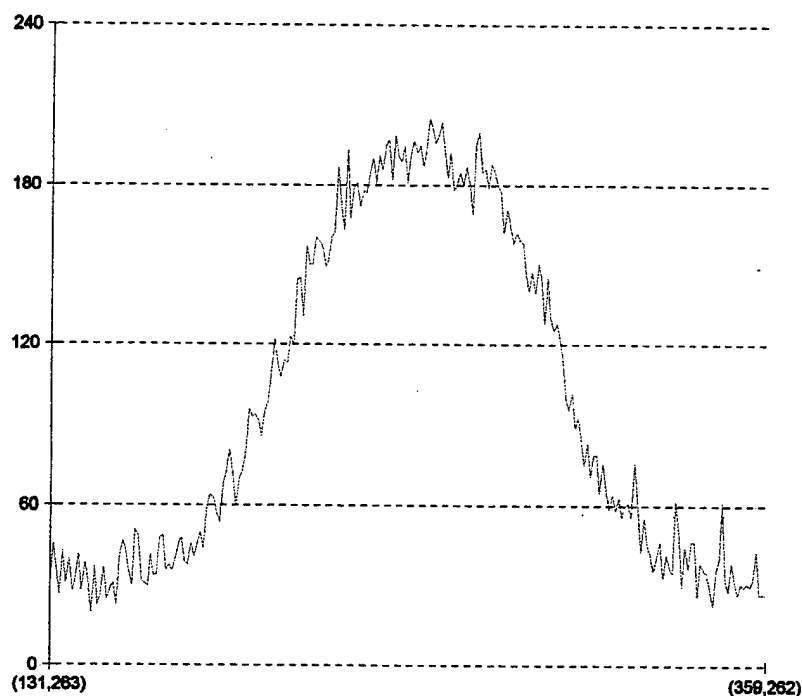


Figure 21. Column average plot of horizontal slice of x-ray image.

Figure 22 shows the column average plot of a vertical slice of the same x-ray image. The fractional fluctuation, intensity amplitude, and width are the same indicating a cylindrically symmetrical radiation pattern. *Image* has a 3-D contour plot, but the contrast magnitude between the background and the x-ray intensity was not adjustable, and the plot was not useful. More recent software programs could provide a more useful 3-D display of the data.

The polycapillary lens was then placed in the target chamber for testing analysis. The same distance was used between the mylar stack and the phosphor screen with the lens placed 250 mm from the cavity. Various pictures were taken with the lens in place. The result is a circular x-ray image roughly the same size (13 mm) as the exit face of the lens. Figure 20 showed the basic false color image of the exiting x-rays. By combining the data for the image without the lens with the data from the image with the lens in place, the characteristics of the lens were examined. Figure 4 was a plot of the relative intensity of the x-ray beam recorded both with and without the lens in place.

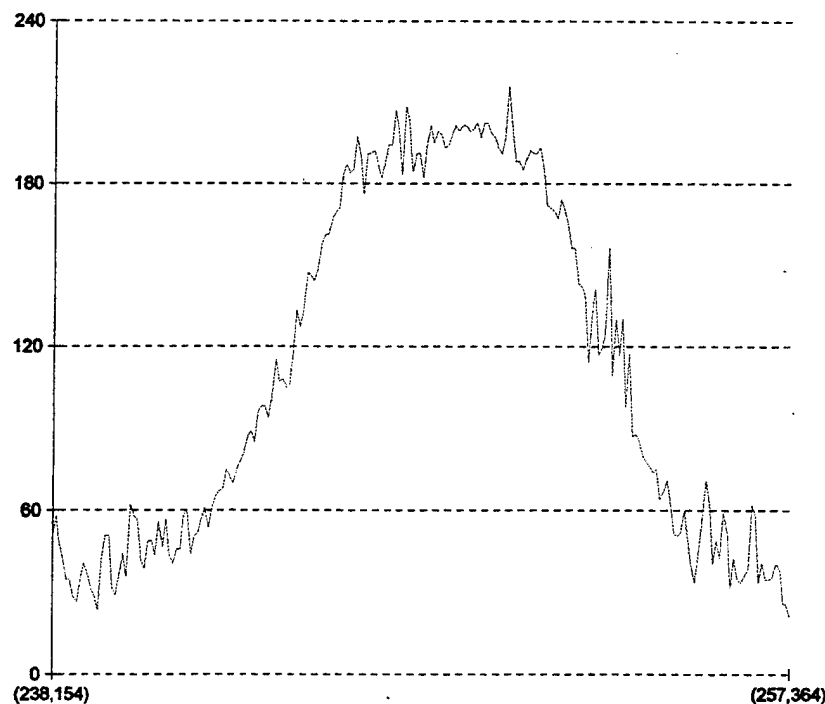


Figure 22. Column average plot of vertical slice of x-ray image.

The relative intensities versus the horizontal position in mm of the image captured without the polycapillary lens in place as well as the plot of the image with the lens in place. The data comes from the column average analysis. The pixel intensity was derived by subtracting the background intensity and inverting the scale to give a positive intensity for the beam. The graph shows that while the general intensity distribution of the image is still Gaussian, the intensity has attenuated by a factor of 0.72.

The polynomial curve fit of the intensity distributions of the images taken both with and without the lens in place normalized in peak intensity to the image without the lens shows that the intensity of 72 occurs with a half-width of 60 pixels for the image without the lens, while the lens shows an intensity of 16 at a half-width of 55 pixels. The lens has reduced 72% of the x-ray intensity, but the transfer of the beam has very effectively retained the spatial intensity distribution.

## B. PARABOLIC MIRROR DATA ANALYSIS

The elliptical image on the screen would have been an 18 mm diameter circle if the mirror was flat. Thus, the convex mirror is a converging lens for x-rays. Using *Image 1.3.2 Software* to produce a column average of pixel intensity reveals the sharp distribution of the x-rays. The pixel intensity ranged from a peak of 212 to a minimum background on 222. Figure 23 is the *Image 1.3.2* analysis of the data of the previous ellipsoidal x-ray image showing the column average plot of intensities.

The highest intensity found occurs on the right side of the center of the reflected x-rays. A symmetrical beam intensity should produce a symmetrical image. The glass mirror was very slightly tapered to fit the narrow end into the magnet. This may have resulted in a slightly non-uniform curvature of the lens due to slight increase in the bending of the smaller glass nearest the magnet compared to the side farthest away from the mirror. Another possibility is that there was a misalignment of the electron beam as it intercepted the stack, creating a slight astigmatism in the x-ray beam. Further experimentation with a symmetrical mirror would determine in the existing mirror is flawed, off center, or if the x-ray beam caused the observed distortion.

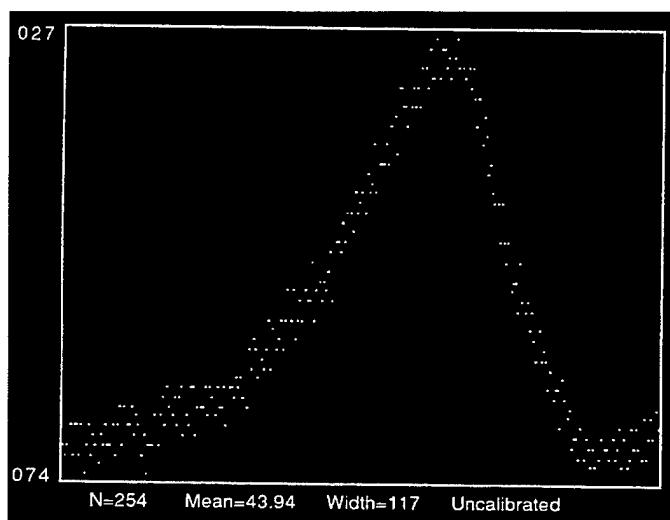


Figure 23. Column average plot of mirror lens image

The fluctuations in the curve are due to the fractional fluctuation of one unit on the intensity scale versus a spread of only ten units of intensity for the image. The intensity is

“smeared out” on the left side of the image compared to the right side. Figure 24 shows a comparison between a flat mirror and a curved mirror on the production of an x-ray image that was originally circular.

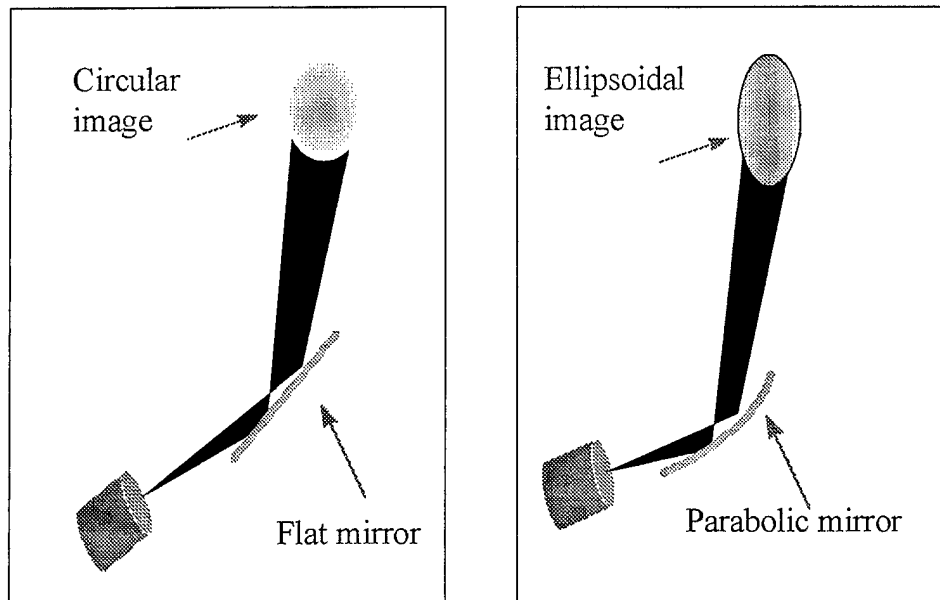


Figure 24. Comparison of flat versus curved mirror projections.

The reflecting mirror has advantages over the polycapillary lens. The mirror technique provides more control over the x-rays. The polycapillary array and the mask would most likely be held in place to coincide with the x-ray source and the resist coated semiconductor would be moved to provide multiple images on the material; however, the parabolic mirror could be mounted such that it rotates in two dimensions to scan x-rays. This has the advantage of providing control over the position of the x-ray beam. The plane of the mask must be normal to the incident x-rays. The mirror could be motorized to rock back and forth to scan x-rays across a mask to ensure uniform exposure rates. If the mirror rotated symmetrically about the axis of x-rays, it would move the reflection in a circle about the reflection angle, providing multiple exposures on a wafer. Figure 25 is a schematic of a theoretical focusing system using transition radiation and a parabolic mirror to step and scan. (Piestrup, 1997)



## A soft x-ray step-and-scan technique

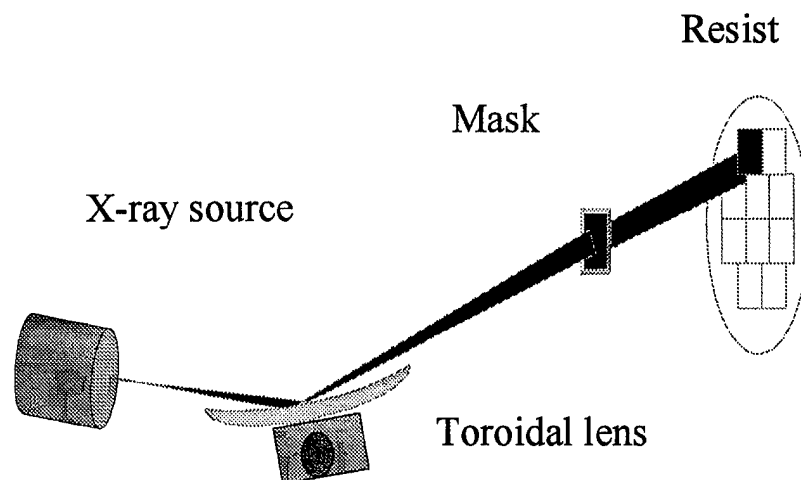


Figure 25. A soft x-ray step and scan technology.

If the parabolic mirror is to be used as a tool to reflect and scan x-rays over the mask, then the intensity of the image and spatial distribution will need to be uniform over the face of the mask. Experiments were performed at the linac that determined the feasibility of rotating the mirror for a scan technique. By defining a fixed area on the phosphor screen and taking a series of digital pictures of the x-ray image as the mirror was rotated from 1.65 to 3.3 degrees, simulating the step-and scan technique. The mirror was rotated to place the image in the center of the screen, a reflection of 3.3 degrees, which is position zero on the figures, and an image was saved for analysis. The mirror was then rotated to move the image over 0.125 to position one and another picture was taken. The mirror was rotated through six positions over total distance of 0.5 inches to accommodate a simulated mask against a resist coated wafer.

The following figures illustrate the characteristics of the scanned images. Figure 26 shows the mean intensity of the column averages over the six positions. The intensity of the x-ray beam reached a maximum in the center position, but was within five units across the entire image in an intensity range of 256 units that the software can differentiate. If the mirror were rotated too far, then the incident angle of the x-rays on the mirror would start to reach and then

ray beam reached a maximum in the center position, but was within five units across the entire image in an intensity range of 256 units that the software can differentiate. If the mirror were rotated too far, then the incident angle of the x-rays on the mirror would start to reach and then exceed the critical angle of total external reflection and the x-ray intensity would decrease due to transmission losses in the glass medium.

### Mean Intensity vs Position

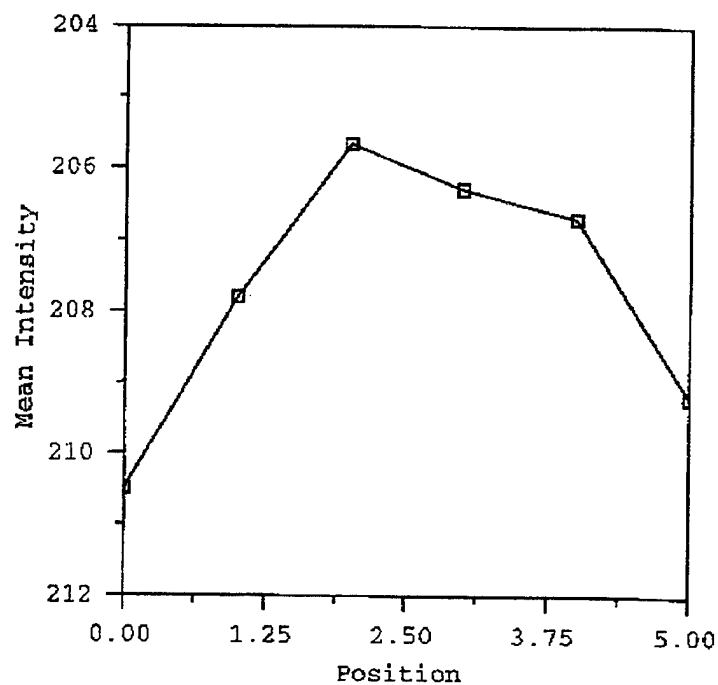


Figure 26. The mean intensity of column averages across six scanned positions.

The peak intensity within the entire image was also determined for each position. If a particular position has a large deviation from the average, then there would be sections on the mask that would receive a larger exposure of x-rays. This could cause unacceptable variances in feature size on the semiconductor device. Some x-ray energy penetrates the mask features and

the level of uniform penetration is important. Figure 27 shows the peak intensity found in a column average for the entire image at each of the six positions.

### Peak Intensity vs Position

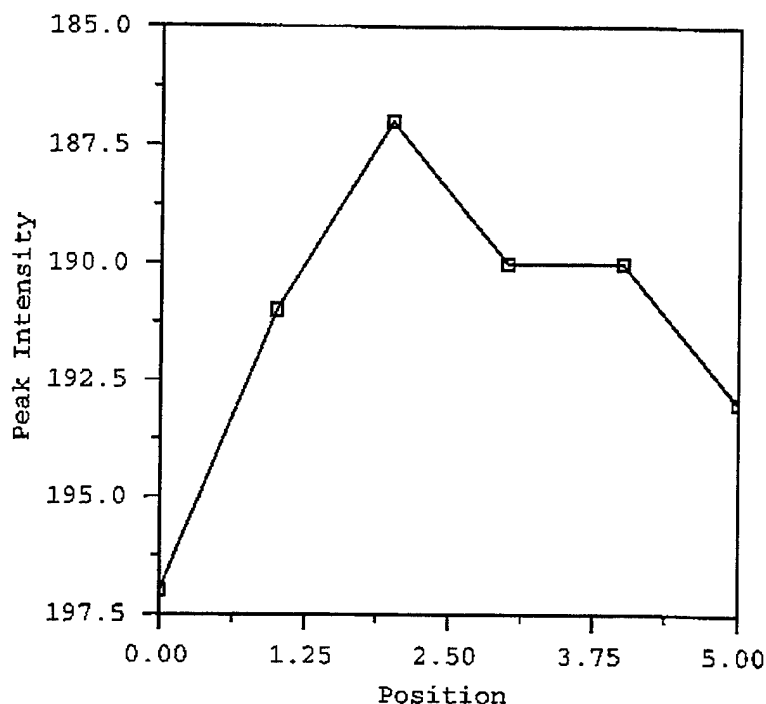


Figure 27. The peak intensity for a pixel column found at each position.

The maximum intensity found for all positions was found at position two. The intensity spike at that position is probably due to random fluctuations in the image on the screen at the moment the digital image was taken. The image visually appeared to be of similar intensity distribution as positions one through four. A larger number of samples should reveal better intensity uniformity due to the reduced fractional fluctuation. The same image pictures were analyzed to determine the range of intensity variation at each position. Figure 28 is a plot of the magnitude of maximum intensity minus minimum intensity found in the entire fixed box area. This data could be extrapolate to provide the x-ray dose that a mask would receive at each

position for a given exposure. Position two has the same maximum that previous figures showed. This is because the plot is made from the same data. Taking additional samples at position two would provide more reliable conclusions.

### Intensity Magnitude vs Position

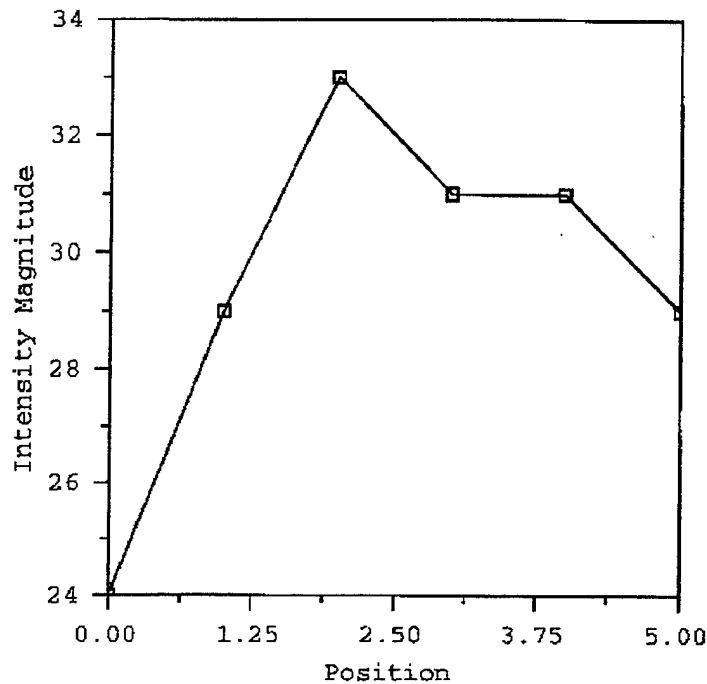


Figure 28. The range of intensities found at each position.

As the position of the image was changed, the overall area of the image varied. By drawing a rectangle around the image at each position, the area of the image was measured. Figure 29 is a plot of area in pixels squared. The area is at a minimum at position one and increases until position three, where it begins to decrease. The larger areas at positions three and four would increase the exposure received if the image was scanned at a constant rate. This increased area offsets the lower peak and mean intensity received at those same positions. The net effect would be a more uniform dose from 0.125 inches to 0.5 inches scanned on the wafer.

## X-Ray Beam Area vs Position

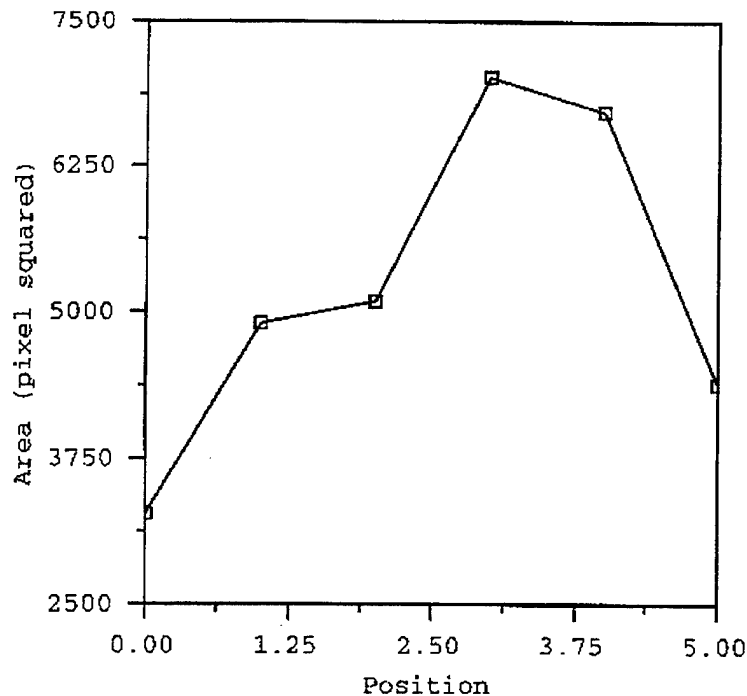


Figure 29. The size of the image at each position in pixels squared.

The particular fixed area on the screen chosen for the previous four plots was a square that was directly in line with the longitudinal axis of the beam. In order to cost effectively manufacture chips, the x-ray beam would need to be reflected up and down, as well as back and forth, to provide more exposures on a given silicon wafer. This particular experiment only examined one dimensions of rotation. Further experiments should test the usefulness of the parabolic mirror. The area of the main x-ray beam on the screen was smaller than the area of the fixed box on the screen. If this beam was used on a circular wafer, then the mirror would be rotated in two coordinates to create exposures across most of the wafer. The mask could also be larger than the size of the x-ray beam, which would require a raster scan across the mask.

The results of the experiment are preliminary, but we demonstrated that conical annular transition radiation can be collected and focused into a parabolic mirror to achieve a scannable x-

ray slit in the laboratory. The cylindrical Gaussian intensity distribution of the cone produced by non-resonant transition radiation provided sufficient planar x-ray uniformity after reflection to warrant further research in order to determine if the technique is suitable for step and scan lithography.

#### IV. CONCLUSIONS

This thesis reports on two innovative methods for collimating, focusing, and deflecting x-rays. The polycapillary lens has been shown to reduce the x-ray beam-spot, in effect, focusing a divergent x-ray beam. It shows promise in this experiment by reducing the geometrical full width half maximum of a projected x-ray beam by 30%. However, the beam is attenuated because the open area on the polycapillary lens face available for x-ray transport is approximately 50% of the total area. In addition, there are apparently other attenuation mechanisms. Oil vapor deposition from the vacuum pumps and absorption internally within the polycapillary walls and perhaps radiation damage are suspect causes for the additional attenuation.

The parabolic mirror defocuses the x-ray beam in one dimension while leaving the other dimension unperturbed. This relatively simple x-ray optic shows tremendous potential for application. The cost of the parabolic mirror is very small compared to the cost of the more complicated polycapillary lens. The experiment in which the beam was moved by mirror rotation demonstrates that this technique can deflect a fixed source of x-rays.

The measurements made here show that other geometries can allow a parabolic mirror type device to be useful for almost all x-ray optics functions. There are practical considerations to be further investigated. However, these initial measurements show promise that optics need not be a limitation to the application of x-rays to lithography.





## APPENDIX A. THE THEORIES AND THE PHYSICS

### A. CHERENKOV VERSUS TRANSITION RADIATION

When a charged particle transverses between two media of different dielectric constants, transition radiation occurs. A normal dipole radiation pattern is Lorentz boosted forward into a conical pattern with an annular shaped pattern impinging on the target. Emission intensity can be increased by stacking thin metal foils or mylar together with spacing between the layers of material. As an electron passes through the stack of foils which have been placed in a vacuum, it encounters sudden interfaces of different dielectric constants and radiates a cone of soft x-rays in the direction of travel. Figure 30 depicts the distortion of mylar molecules as electrons transit the material. An incoherent x-ray pattern is formed when random spacing exists in the radiator cavity, such as one made of foam. A coherent radiation pattern results when the spacing between layers and the thickness of the layers is carefully constructed. Resonant Transition Radiation results when the cavity design correctly matches the velocity of the electrons passing through and produces an interference pattern. (Wartski, 1976)

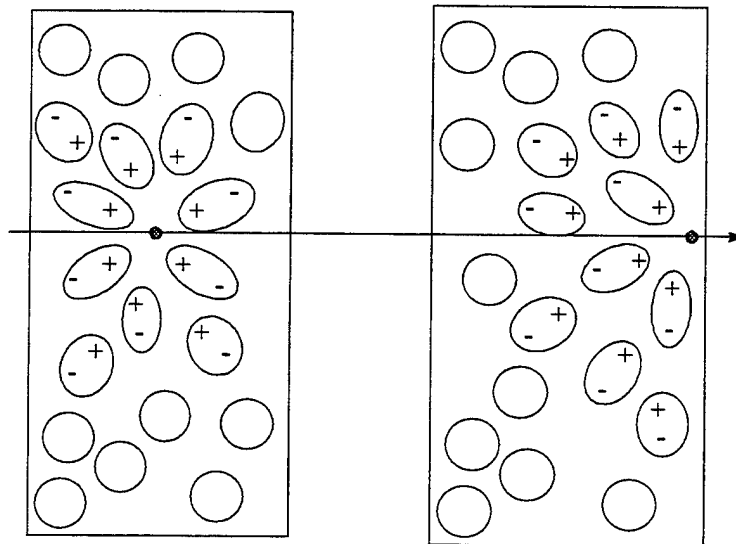


Figure 30. Electrons transiting mylar strips in a vacuum.

the medium along its track to be momentarily polarized thus generating a short electromagnetic pulse as it passes through each layer of material. The fields then propagate as radiation at the Cherenkov angle,

$$\cos\theta_c \equiv \frac{c/n}{v}, \quad (10)$$

where  $c$  is the speed of light in a vacuum,  $n$  is the index of refraction of the medium, and  $v$  is the phase velocity of light in the medium. Cherenkov radiation takes the shape of a cone, or annulus in three dimensions. The intensity varies with frequency and is difficult to detect at microwave frequencies unless an intense bunched electron beam is used. (Wartski, 1976)

Transition radiation occurs when a charged particle of constant speed passes through a boundary separating media of two different electromagnetic properties, which is illustrated in figure 31. When the boundary is abrupt, such as between a conductor and a dielectric, transition radiation is dependent on the trajectory of the particle and the intensity is strongly dependent on the energy of the particle. (O'Grady, 1986)

The initial experiments were conducted at the Naval Postgraduate School Linear Electron Accelerator using a radiator stack designed to generate coherent transition radiation. The stack consisted of twenty-three concentric aluminum washers cut from a flat sheet of the same thickness. Type "C" Mylar (Trademark of E. I. Dupont de Nemours, Inc.) was placed between each ring and the assembly was bolted together. Different stacks were also used that contained 40 and 60 layers during the course of the experiments. The resonant stack contained layers with a nominal Mylar thickness of 3.5 microns and a washer thickness of 8.5 microns.

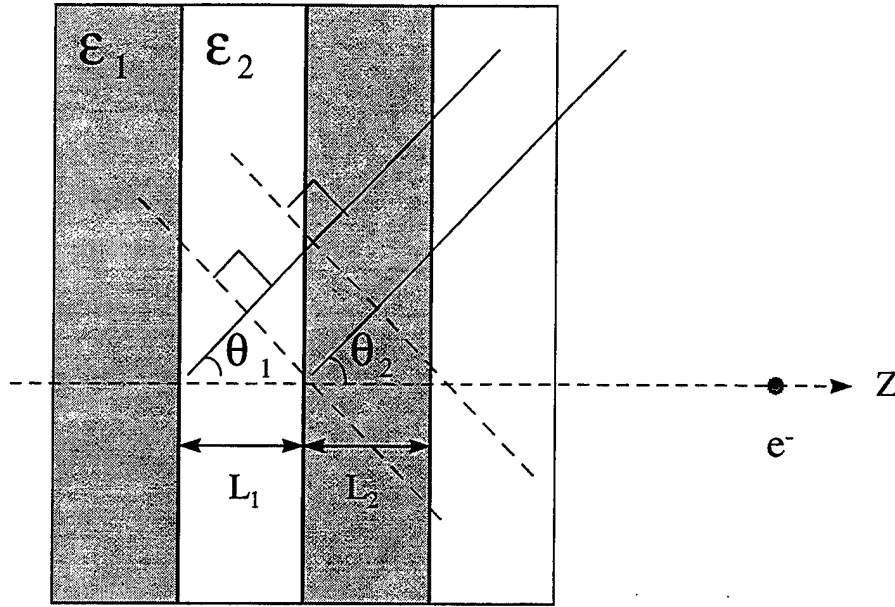


Figure 31. Transition radiation parameters.

The total energy lost by transition radiation is proportional to the Lorentzian factor  $\gamma$ , for the electron and is given by

$$\gamma = \left(1 - \frac{v^2}{c^2}\right)^{-1/2} = \frac{E}{mc^2} \quad (11)$$

where  $v/c$  is the reduced velocity of the electron to the speed of light in a vacuum,  $E$  is the electron's total energy, and  $mc^2$  is its rest energy. (Piestrup, 1992)

Consider the differences between Cherenkov and transition radiation. Let us assume constant velocity by an electron passing through a medium. The simplest model bases interactions with the medium collectively due to macroscopic properties of permittivity  $\epsilon$  and permeability  $\mu$  and not on an atomic level of individual atoms. Consider a homogenous, indefinite medium that is transversed by the electron, and we can see that the atoms in the medium become polarized by the negative charge of the electron (Figure 30). The electron cloud of the atoms become distorted into dipoles that collapse into their equilibrium shape after the electron passes, producing a symmetrical electromagnetic field with zero amplitude in the far field. If the particle were to pass into the medium at the speed of light, the atoms in front of the

particle would not be as distorted as the ones behind the particle, and the far field electromagnetic field would not be zero. A particle does not radiate if the velocity is constant, unless that velocity is equal to the phase velocity of the radiated wave in the direction of propagation. Cherenkov radiation is produced when the velocity of a particle is greater than the speed of light in that medium. The Cherenkov relationship for an infinite medium can be written as:

$$\cos \theta = \frac{1}{\left(\frac{v}{c}\right)n} \quad (12)$$

where  $n$  is the refractive index of the medium. When the medium is inhomogeneous or when the particle passes through an interface between media of different permittivities, there is a resulting dipole moment that is not zero, regardless of the particle velocity. This is known as transition radiation. Emission can be increased by adding multiple interfaces, either randomly as in a foam plastic, or periodically in a stack of layered material. (Piestrup, 1992)

## B. TRANSITION RADIATION THEORY

The minimum distance over which a charged particle and an electromagnetic wave can exchange energy is called the formation length and is determined by

$$z_i = \frac{2c}{\omega \left[ 1 - \frac{v}{c} \left( \varepsilon_i - \sin^2 \theta \right)^{1/2} \right]} \quad (13)$$

where  $\varepsilon_i = 1 - (\omega_i / \omega)^2$ ,  $\omega$  is the plasma frequency, and  $\theta$  is the angle of radiation emission. Since the plasma frequency of a material is proportional to the square root of its density, and the cutoff frequency is proportional to the plasma frequency, it follows that the cutoff frequency is proportional to square root of the foil density (Votruba, 1991). There will be transition radiation when  $l_1$  or  $l$  are greater than their respective  $z_i$ . Due to the relativistic electrons, a Lorentz contraction of the radiation emits the x-rays in a cone in the direction of propagation. The

distribution from a random foil radiation pattern is in the form of an annulus with peak x-ray emission occurring at  $\theta_{apex} \equiv \sqrt{1 - \frac{v}{c}}$ . The differential cross section for transition radiation production per photon-energy interval per solid angle is a function of three factors:

$$\frac{d^2 N(\omega)}{d\omega d\Omega} = F_1 F_2 F_3, \quad (14)$$

where  $N(\omega)$  is the number of x-ray photons and  $\omega$  is their radial frequency. The  $F_1$  factor is the contribution from a single interface and is given by:

$$F_1 = \frac{(1/137)\omega \sin^2 \theta}{16\pi^2 c^2} (z_1 - z_2)^2. \quad (15)$$

The  $F_2$  factor accounts for the coherent superposition of radiation from the two surfaces present on each foil. A optical analogy for  $F_2$  would be the constructive interference from a single slit diffraction experiment.

$$F_2 = 4 \sin^2 \frac{l_2}{z_2}, \quad (16)$$

where  $l_2$  is the foil thickness and  $z_2$  is the formation length in the medium. The formation lengths can be determined from the following formula:

$$z_{1,2} = \frac{4\lambda}{\frac{1}{\gamma^2} + \frac{\omega_{p1,2}^2}{\omega^2} + \theta_r^2}. \quad (17)$$

The  $F_3$  factor accounts for the contribution of the total number,  $N$ , of foils in the stack:

$$F_3 = \frac{\sin^2 N \left( \frac{l_1}{z_1} + \frac{l_2}{z_2} \right)}{\sin^2 \left( \frac{l_1}{z_1} + \frac{l_2}{z_2} \right)}. \quad (18)$$

If the foil stack is periodic, the maximum energy exchange occurs when the ration of  $l$  to  $z_2$  is a half multiple of  $\pi$  and  $\frac{l_1}{z_1} + \frac{l_2}{z_2}$  is an integer multiple of  $\pi$ , such that :

$$\frac{d^2 N(\omega)}{d\omega d\Omega} = 4N^2 F_1. \quad (19)$$

These are the two conditions for *resonant* transition radiation where radiation from all the surfaces occurs in-phase. If the distances in thickness are random, then the radiation is not in phase and

$$F_3 = \frac{1 - e^{(-N/137)}}{1/137}. \quad (20)$$

This form of  $F_3$  takes the average photon attenuation into account. The resonant condition becomes:

$$\cos \theta_{es} = \frac{l_1 + l_2}{\sqrt{\epsilon_1 l_1} + \sqrt{\epsilon_2 l_2}} \left\{ \frac{1}{\beta} - \frac{\lambda r}{l_1 + l_2} \right\}. \quad (21)$$

The peak emission angle for the incoherent case decreases as the electron beam velocity increases. The emission angle for the incoherent stack is a function primarily of the plasma frequency of the foil and is given by:

$$\theta_{stack}^2 = \frac{1}{3} \left[ -(\gamma_1 + \gamma_2) + \sqrt{(\gamma_1 + \gamma_2)^2 + 12\gamma_1 \cdot \gamma_2} \right], \quad (22)$$

$$\text{where } \gamma = \frac{1}{2(\sqrt{c})^2} + \frac{\omega_i^2}{2\omega^2}. \quad (23)$$

Since the interfoil gas is a vacuum in this experiment,  $\omega_i = 0$ , and the spectral density per unit of solid angle can be expressed as the integral along the trajectory of a moving charge:

$$\frac{d^2\omega}{d\omega d\Omega} = \frac{a^2\omega^2\sqrt{\epsilon}}{4\omega^2c^3} \left| \int (\vec{n} \times \vec{v}(t)) \cdot e^{i(\omega t - \vec{k}r(t))} dt \right|^2. \quad (24)$$

(Piestrup, 1992, and Wartski, 1976)

### C. SNELL'S LAW OF REFLECTION AND REFRACTION

As we examine the propagation of x-rays that cross through media of different electrical properties that change in a discontinuous manner, we will see that the transverse electromagnetic wave will experience reflection at the boundary. Waves that are transmitted across the boundary undergo a change in their propagation direction known as refraction. In Figure 32 the incident ray both reflects and refracts into the medium. In this section we will derive the laws of reflection and refraction relying on the wave properties of light. Then we will use the boundary conditions developed in Maxwell's equations to determine the amplitude of light waves reflected and refracted. This will show that the fraction of a wave that is reflected and transmitted at the boundary separating media is proportional to the velocity of the wave in the two media. There is an angle that will reflect only linearly polarized light known as the Brewster's angle. There is also an angle that will totally reflect all light waves incident upon a boundary known as the critical angle. (Gunther, 1990)

The mathematical basis for total external reflection used in this thesis follows the derivation and discussion found in Gunther's text on Modern Optics.

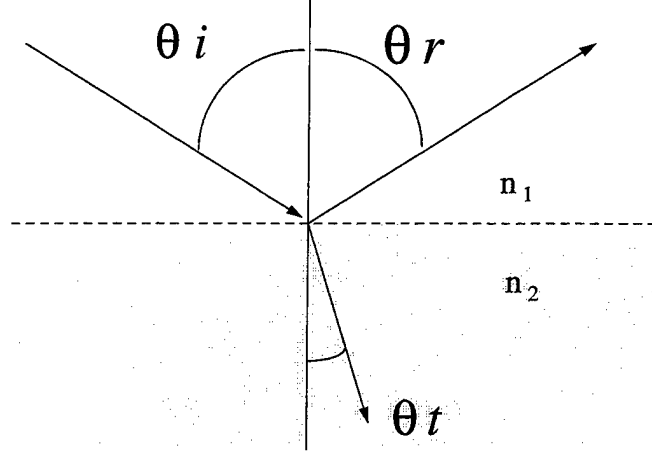


Figure 32. Reflection and refraction.

$E = E_0 e^{i(\omega t - \vec{k} \cdot \vec{r})}$  implies a plane wave incident on a non-conducting transmitting medium. For the boundary conditions to be satisfied for all time, the exponentials are the same for the boundaries of all three field (incident, reflected, and transmitted). Therefore, the phases must be the same and  $\omega_i t - \vec{k}_i \cdot \vec{r} = \omega_r t - \vec{k}_r \cdot \vec{r} = \omega_t t - \vec{k}_t \cdot \vec{r}$  on the boundary at all times. Which is true if  $\omega_i = \omega_r = \omega_t$  and  $\omega$  must be the same. So  $\vec{k}_i \cdot \vec{r} = \vec{k}_r \cdot \vec{r} = \vec{k}_t \cdot \vec{r}$ . Define  $\hat{n}$  such that  $\hat{n} \cdot \vec{r} = 0$ .

$$\begin{aligned}
 \hat{n} \times (\hat{n} \times \vec{r}) &= (\hat{n} \cdot \vec{r}) \hat{n} - \vec{r} (\hat{n} \cdot \hat{n}) \\
 \vec{r} &= -\hat{n} \times (\hat{n} \times \vec{r}) \\
 \vec{k}_i \cdot \vec{r} &= -\vec{k}_i \cdot (\hat{n} \times (\hat{n} \times \vec{r})) = -(\hat{n} \times \vec{r}) \cdot (\vec{k}_i \times \hat{n}) \\
 (\vec{k}_i \times \hat{n}) \cdot (\hat{n} \times \vec{r}) &= (\vec{k}_r \times \hat{n}) \cdot (\hat{n} \times \vec{r}) = (\vec{k}_t \times \hat{n}) \cdot (\hat{n} \times \vec{r}) \\
 \text{implies } \vec{k}_i \times \hat{n} &= \vec{k}_r \times \hat{n} = \vec{k}_t \times \hat{n}.
 \end{aligned} \tag{25}$$

Therefore,  $\vec{k}_i, \vec{k}_r, \vec{k}_t$ , and  $\hat{n}$  are coplanar.

$$\left. \begin{aligned} |\vec{k}_i \times \hat{n}| &= \vec{k}_i \sin \theta_i \\ |\vec{k}_r \times \hat{n}| &= \vec{k}_r \sin \theta_r \\ |\vec{k}_t \times \hat{n}| &= \vec{k}_t \sin \theta_t \end{aligned} \right\} \Rightarrow \vec{k}_i \sin \theta_i = \vec{k}_r \sin \theta_r = \vec{k}_t \sin \theta_t \tag{26}$$

$$\text{Therefore } \vec{k}_i \sin \theta_i = \vec{k}_r \sin \theta_r, \quad \text{and } \underline{\theta_i = \theta_r}. \tag{27}$$



$$\text{If } k_i \sin \theta_i = k_t \sin \theta_t \quad \text{and} \quad k = \frac{n}{c} \omega, \quad (28)$$

$$\text{then } \underline{n_i \sin \theta_i = n_t \sin \theta_t} \quad (\text{Snell's Law}). \quad (29)$$

For the special case where  $n_t > n_i$  and  $\theta_r + \theta_t = \pi/2$ , the reflected wave is linearly polarized and this angle is known as the *Brewster's angle*. We are interested in the special case where  $\theta_t = \pi/2$ , and  $\sin \theta_i = n_t/n_i$ . This angle is known as the *critical angle*. Light and x-rays incident upon a surface at angles greater than the critical angle experience total external reflection and there is no transmitted wave. Total reflection occurs whenever  $\theta_{\text{critical}} \leq \theta_i \leq \pi/2$ .

$$\begin{aligned} \vec{k}_i &= k_i (\hat{i} \sin \theta_i - \hat{k} \cos \theta_i) \\ \text{The Incident Wave Vector} \quad \vec{E}_i &= E_{pi} (\hat{i} \cos \theta_i + \hat{k} \sin \theta_i) + E_{ni} \hat{j} \end{aligned} \quad (30)$$

$$\begin{aligned} \vec{k}_r &= k_r (\hat{i} \sin \theta_i + \hat{k} \cos \theta_i) \\ \text{The Reflected Wave Vector} \quad \vec{E}_r &= E_{pr} (-\hat{i} \cos \theta_i + \hat{k} \sin \theta_i) + E_{nr} \hat{j} \end{aligned} \quad (31)$$

$$\begin{aligned} \vec{k}_t &= k_t (\hat{i} \sin \theta_t - \hat{k} \cos \theta_t) \\ \text{The Transmitted Wave Vector} \quad \vec{E}_t &= E_{pt} (\hat{i} \cos \theta_t + \hat{k} \sin \theta_t) + E_{nt} \hat{j} \end{aligned} \quad (32)$$

The appropriate boundary conditions associated with Maxwell's equations are as follows:

1. Because  $\nabla \cdot \vec{D} = \rho$ , the normal components of the D field must be continuous since there are no charges on the dielectric surface. The boundary condition and the dot product of its components reveals that:

$$\begin{aligned} [\epsilon_i (E_i + E_r) - \epsilon_t (E_t)] \cdot \hat{n} &= 0 \\ \epsilon_i \sin \theta_i (E_{pi} + E_{pr}) &= \epsilon_t \sin \theta_t E_{pt} \end{aligned} \quad (33)$$

2. Because  $\nabla \times \vec{E} = -\partial \vec{B} / \partial t$ , the tangential component of the E field must be continuous. This boundary condition and the cross product of its components reveals:

$$\begin{aligned} \vec{E} \times \hat{n} &= E_y \hat{i} - E_x \hat{j} \\ (E_{ni} + E_{nr} - E_{nt}) \hat{i} - (E_{pi} \cos \theta_i - E_{pr} \cos \theta_i - E_{pt} \cos \theta_t) \hat{j} &= 0 \end{aligned} \quad (34)$$

which has vector components that must equal zero so:

$$\begin{aligned} E_{ni} + E_{nr} &= E_{nt} \\ (E_{pi} - E_{pr}) \cos \theta_i &= E_{pt} \cos \theta_t \end{aligned} \quad (35)$$

3. Because  $\nabla \cdot \mathbf{B} = 0$ , the normal component of the B field must be continuous. This boundary condition is written as:

$$\begin{aligned} [\bar{\mathbf{B}}_i \cdot \hat{\mathbf{n}} + \bar{\mathbf{B}}_r \cdot \hat{\mathbf{n}} - \bar{\mathbf{B}}_t \cdot \hat{\mathbf{n}}] &= 0 \\ \text{and because } \bar{\mathbf{B}} &= \left( \frac{\sqrt{\mu\epsilon}}{k} \right) \bar{\mathbf{k}} \times \bar{\mathbf{E}} \end{aligned} \quad (36)$$

$$4. (\mathbf{E}_i + \mathbf{E}_r + \mathbf{E}_t) \times \hat{\mathbf{n}} = 0$$

The transmitted wave becomes imaginary at angles greater than the critical angle:

$$\cos \theta_t = \sqrt{1 - \sin^2 \theta_i} = \sqrt{1 - \left( \frac{n_i}{n_t} \right)^2 \sin^2 \theta_i} = \sqrt{1 - \frac{\sin^2 \theta_i}{\sin^2 \theta_{critical}}} \quad \text{and} \quad \cos \theta_t = i \sqrt{\frac{\sin^2 \theta_i}{\sin^2 \theta_{critical}} - 1} \quad (37)$$

The transmitted wave propagates parallel to the surface of the medium and is attenuated exponentially in the normal direction. This is called an inhomogeneous plane wave that is not transverse. The coefficients of reflection are:

$$\begin{aligned} R_s &= \frac{\tan^2(\theta_i - \theta_t)}{\tan^2(\theta_i + \theta_t)} = \frac{\tan^2(\theta_i - \pi/2)}{\tan^2(\theta_i + \pi/2)} = \frac{\cot^2 \theta_i}{\tan^2 \theta_i} = 1 \\ \text{and } R_p &= \frac{\sin^2(\theta_i - \theta_t)}{\sin^2(\theta_i + \theta_t)} = \frac{\sin^2(\theta_i - \pi/2)}{\sin^2(\theta_i + \pi/2)} = \frac{\cos^2 \theta_i}{\cos^2 \theta_i} = 1 \end{aligned} \quad (38)$$

(Gunter, 1990). Figure 33 is a Matlab plot of the perpendicular and parallel reflection coefficients.

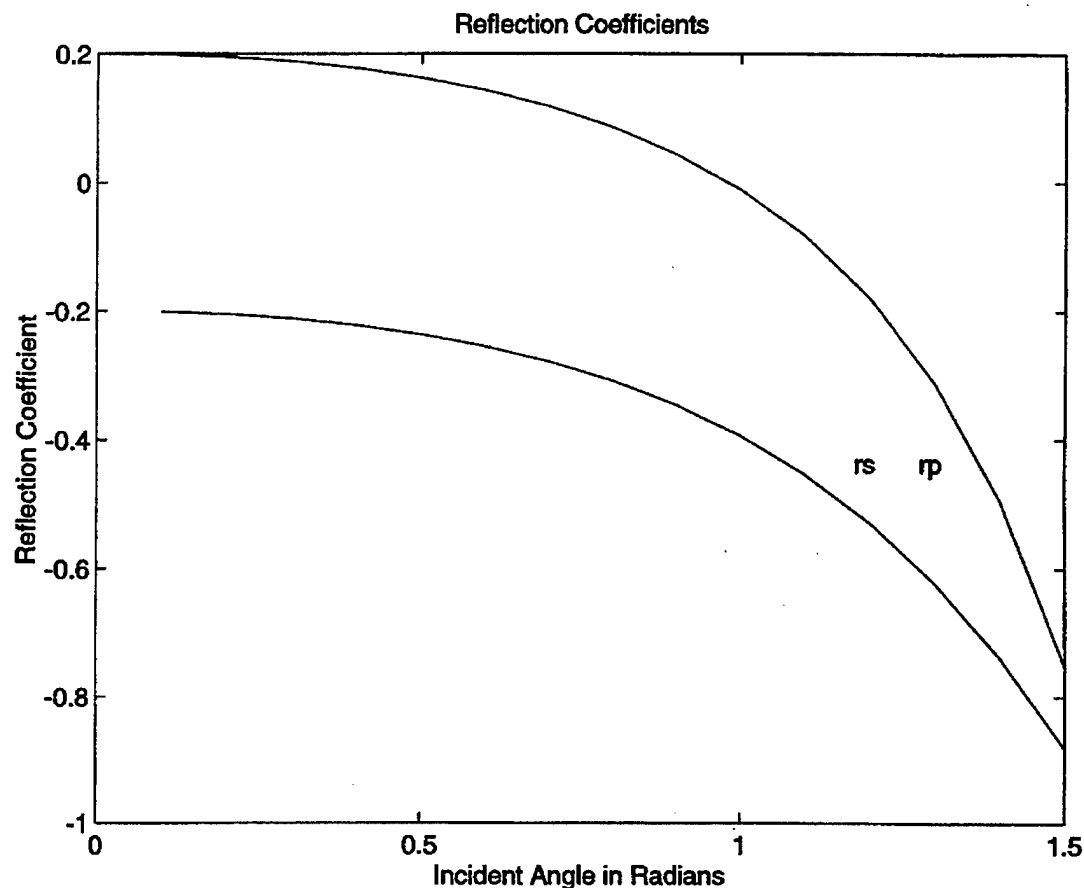
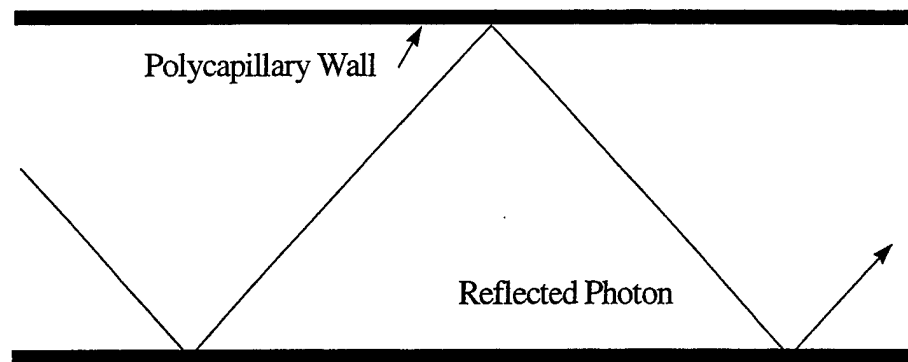


Figure 33. Parallel and perpendicular reflection coefficients.

#### D. POLYCAPILLARY WAVEGUIDE OPTICS

A flat plate can be used to reflect x-rays provided the angle of incidence is greater than the critical angle. If two plates are parallel to each other, a channel can be formed for transporting the x-rays. The number of reflections will attenuate the x-rays and it is desirable to have a very high angle of incidence to increase the horizontal propagation of the x-rays. A waveguide can be formed using a rectangular or circular channel that will continue to reflect the x-rays in a geometric fashion. The loss of x-ray intensity as the bundle of photons propagates is proportional to the reflectivity of the material raised to the power equal to the number of times

the bundle reflects off the channel walls:  $I_{loss} \propto R^n$ . Figure 34 is a diagram showing propagation of photons between parallel plates.



#### Total External Reflection of X-Rays in Straight Polycapillary

Figure 34. Reflection propagation between two plates.

The waveguide can also be curved to redirect the average direction of propagation of the bundle of photons. Provided each grazing angle remains greater than the critical angle and the attenuation losses are small at each reflection, an array of glass capillaries can be used to collimate a diverging source of x-rays into a nearly parallel beam. Figure 35 shows a curved waveguide. (Klotzko, 1996)

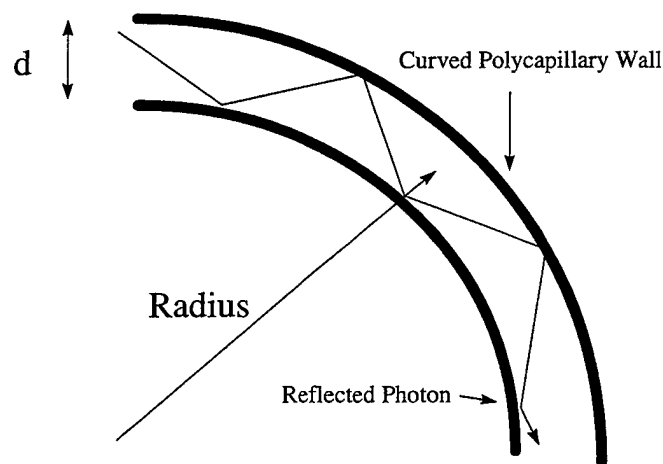


Figure 35. Reflection propagation in a curved capillary.

In order to achieve a maximum transport of x-rays, the angle of incidence must be as shallow a grazing angle as possible entering the array of capillaries. This will equate to a narrow cone of divergence of x-rays from the source or a greater distance from a low gain source. Reflections off a very large radius of curvature waveguide will approach reflections off flat plate model. If we begin increasing the curvature of the capillaries we are decreasing the angle of incidence for adjacent reflections. The rays will cease to propagate when the angle decreases below the critical angle, thereby increasing transmission into the walls of the channel and attenuating the beam.

The maximum radius of curvature permitted for total external reflection to occur throughout our capillary is proportional to the diameter of the capillary, the wavelength of the x-rays, and the index of refraction of the capillary material. Figure 36 shows the geometry used to determine the maximum bending allowed for polycapillary waveguide propagation. (Klotzko, 1996)

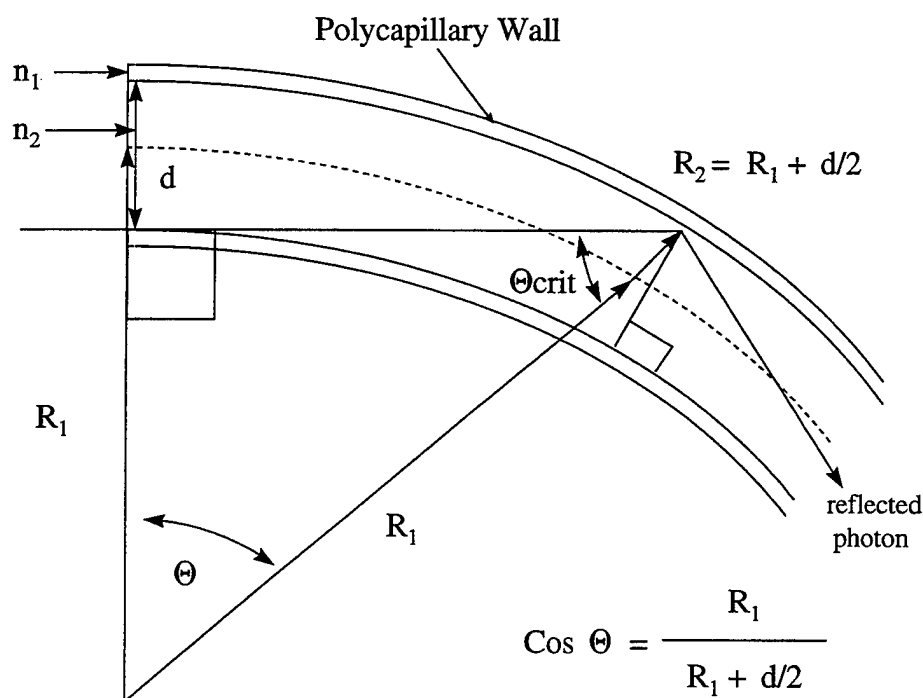


Figure 36. Critical angle in a curved polycapillary.

The light rays shown here have entered the polycapillary in the longitudinal direction of propagation with zero angle of incidence. An ideal polycapillary will propagate the ray without transmission losses as long as the angle of incidence inside the now curved polycapillary does not exceed the critical angle. Figure 36 shows the geometry for determining the maximum curvature of radius that will allow the critical angle to be maintained. Light incident normal to the face plane of the capillary will travel in the intended direction until the curvature exceeds the interior diameter of the capillary. It will then reflect off the surface of the glass. Light entering the channel at incident angles less than the critical angle will transmit into the waveguide with anticipated transmission losses at each reflection until attenuated. And light entering the channel at angles greater than the critical angle will transmit without losses due to total external reflection as long as the curvature does not induce reflection angles less than the critical angle. The critical angle is therefore the acceptance angle for our waveguide for useful propagation distances. (Gunther, 1990)

In addition to meridional rays (rays which cross the central optical axis), the polycapillary will also propagate skew rays (a ray that lies in a plane not containing the axis). An x-ray can propagate down the channel in a series of reflections that looks like a squared off corkscrew pattern. A skew ray propagates in a plane between each set of reflections that forms an angle  $\phi$  with the central axis. The component of the ray that propagates parallel to the normal vector of the glass is  $k_i \cos\phi \sin\theta_i$ . The normal vector is the radius vector from the cylindrical axis of the polycapillary to the point where the x-ray strikes the glass surface, which forms our angle of incidence. The component of the ray along the normal is  $k_i \cos\theta_2$ . As long as  $\theta_2$  is equal to the critical angle, then  $\cos\phi \sin\theta_i = \sqrt{1 - n_1^2}$ . Thus, for a skew ray the minimum acceptance angle is equal to the maximum acceptance angle for a meridional ray. The skew rays act to increase the flux of the polycapillary. (Gunther, 1990)

The symmetrical propagation of the x-rays through the waveguide about the axis indicates that the output angle of each x-ray will be equal to the input incident angle. The output plane of the meridional rays does not change upon exiting the capillary, but the skew rays exit at a position that is a function of the number of reflections. Therefore the skew rays act to uniformly distribute the exiting x-rays about a circle of radius equal to their input radius.

## APPENDIX B. LITHOGRAPHY APPLICATIONS

### A. POLYCAPILLARY LENS USE IN X-RAY LITHOGRAPHY

X-ray lithography is technically feasible, but expensive. The small wavelength of x-rays can provide better resolution than optical or ion beam lithography, which equates to smaller features on semiconductor devices. But there are physical limits to the minimum feature size possible for a semiconductor device. The technical challenges include reliable x-ray sources, lowering defects in the mask, making accurate alignment of overlays, and developing suitable resists. Because of the short wavelengths, diffraction and depth of focus problems will not plague the x-ray lithographer. Additionally, many of the impurities that cause defects on optical masks are transparent to x-rays. (Klotzko, 1996)

Optical lithography is limited to sub-micron dimensions due to four specific problems: depth of focus, fabrication resolution, field size versus lens resolution, and optical wavelength lower limit. Depth of focus can be defined as:  $DOF = (\text{minimum line-width})^2 / \text{wavelength}$ . It is the magnitude of the displacement of the wafer that causes the image of the mask to be blurred by one unit of minimum resolution. For a given wavelength, to decrease the line-width, the DOF must decrease by the square of the square of the line-width. The fabrication resolution limit determines the minimum feature size on a device. The minimum feature size  $F_{\min} = 0.75 (\text{wavelength}) / (\text{numerical aperture of the lens})$ . The lens quality and the wavelength of the light are currently the limiting factors. The ratio of the field size to the minimum feature resolvable is nearly constant for all lenses, consequently a given lens cannot produce a higher density integrated circuit for a constant chip size. The spherical and sagittal aberrations increase to the 8th and 4th power of the lens numerical aperture respectively. Additionally, the transparency of the glass used in micro-lithography decreases below 300 nm light. The material properties of the lens therefore can limit the resolution available optically. (Ruddell, 1985)

Electron beam lithography can overcome many of the limitations of optical lithography; however, it is limited by system complexity, electron scattering effects, beam shaping requirements, and beam throughput versus minimum feature size tradeoffs (Piestrup, 1987). But

it has found a market making masks and testing advanced circuit designs. The most challenging aspect to electron beam systems is the spatial current density distribution of the beam shape. A Gaussian beam needs to be scanned across the mask, perhaps several times, to ensure a uniform illumination on the resist. Electron beams can also be shaped using quadrapole magnets to alter the intensity distribution of the x-rays coming from the stack.

## **B. THE STEPS IN THE LITHOGRAPHIC PROCESS**

The lithographic process is described in detail in Dammel's primer on photoresists. This section is a summary of the steps listed in his text. The first step in the physical process of lithography is to prepare the substrate for the resist. Wafers are heated to above 150 °C to remove adsorbed moisture and to treat them with gaseous hexamethyldisilazane (HMDS), which promotes adhesion., followed by an N<sub>2</sub> purge with additional heating. An alternative hydrophobic preparation is to dip the silicon wafers in a dilute HF solution.

The next step is to spincoat the wafers with liquid photoresist. A precise, thin film resulting from a high spin speed will equate to high resolution, but must be taken to maintain a uniform layer of chemical despite vibration induced striations. An acceleration caused by 2 x 10<sup>4</sup> rpm will reduce the striations in the surface to less than 10 nm.

The resist is converted from a liquid cast film into a solid film by a pre-exposure bake. Typical conditions are 30 min at 80 °C in forced air ovens. During all of these pre-exposure steps the wafer surface and resist are highly sensitive to chemical and particle contamination.

The optical apparatus used to expose the resist is usually a complex and expensive stepper tool. The time that a wafer is exposed is also a complex variable that depends on the chemistry of the pre-bake steps, the intensity of the optics, the tone of the system being produced (positive or negative), and the properties of the resist. In general, there is a linear increase in exposure time for the increasing thickness of the resist. One of the most important resist compounds used today is called diazonaphthoquinone (DNQ). It has a sensitivity swing curve for the dose based on the resist thickness. Depending on the desired shape of the edges at the top of the resist material, the dose varies sinusoidal. This is due to thin film interference effects and



causes periodic striations inside the resist structures from standing waves set up during the exposure period. This variation can be used to provide T-topping, 90° edges, or rounded tops.

A pre-development bake is usually performed to reduce the striations caused by the standing wave patterns along the sides of the resist. These striations would not appear until after development. This post exposure bake also enhances the sensitivity of the resist to development.

The resist is then developed. There is some latitude in trading off development time and exposure time, but the development time should be sufficient to remove all of the resist residues in the desired areas. A positive-tone resist development removes material from the exposed resist area. Over-development can result in edge lifting under the non-exposed areas adjacent to the exposed ones and can overly round off the edges of an otherwise correctly developed boundary. One technique used to apply the developer is called "double puddle" development. It starts by spraying the chemical on until a puddle forms, allows 12 seconds for development, spins the wafer to remove the developer, and then sprays on a new puddle, and spin removes the developer after 32 seconds. This produces straighter profiles in the resist.

Following development, the wafer can be baked in a forced air oven or on a hot-plate. This removes any remaining solvent, increases the level of adhesion between the resist and the substrate, and hardens the resist structures. The resist is now properly set on the substrate and will act as the template for the dry etch, which will remove material from the substrate that is not covered with resist. After the desired amount of substrate has been etched away, the resist is no longer needed and is removed using solvents called strippers. (Dammel, 1993)

### C. X-RAY LITHOGRAPHY

X-ray lithography does not use reducing optics between the mask and the photoresist layer on a wafer. This is known as 1X proximity lithography. The mask must be carefully constructed because it will need to have the same size features that will be formed on the wafer. In 5X optical lithography, the mask is reduced along with the errors, but in 1X, the errors remain the same size. The resist used in X-ray lithography is a thin film of organic material that is deposited on a semiconductor wafer on which a dielectric or metal layer is implanted. In a *positive resist* process, the resist is soluble and interacts with radiation to become insoluble. The

reverse is possible in a *negative resist* process that produces soluble areas in a formerly insoluble material. Following x-ray exposure, a post-exposure bake produced the correct tone on the resist, then an aqueous solution rinse removes the appropriate resist material, followed by a plasma etch to remove metallic layer portions from the wafer. There are four primary characteristics to the x-ray beam that effect the quality of the circuit on the wafer: local divergence, global divergence, intensity, and uniformity. (Klotzko, 1996)

Local divergence is caused by Fresnel diffraction of the x-ray radiation as it passes through the mask. Each edge of the mask experiences a knife edge diffraction pattern. X-rays are attenuated and phase shifted at the edge. Due to the incoherent radiation incident on the edge, the diffraction pattern has a blurred edge and not the familiar fringed boundary Fresnel pattern of alternating high and low intensity lines from a laser passing through a slit. The blurred region should not exceed 50% of the minimum desired feature size and reduces the resolution but limits the diffraction pattern. (Klotzko, 1996)

Global divergence occurs because of the x-ray divergence from the source. Any distance between the source and the wafer will exacerbate the divergence effects on the resist. This increasing of the angle of incidence of the x-rays as we move away from the normal position on the wafer creates larger features on the resist. X-rays are not perfectly absorbed in the material of the mask and a strong x-ray source can produce undesirable defects on the resist due to the diffraction effects. (Ruddell, 1985)

## APPENDIX C. THE NPS LINEAR ACCELERATOR

### A. INTRODUCTION TO THE LINAC

The electron linear accelerator at the Naval Postgraduate School was constructed from materials used in a prototype accelerator at Stanford University in 1965 and began initial operations in January 1966. It achieved full capability later that year and was used initially for radiation damage studies and nuclear structure research. The accelerator, with the exception of the end station, was put together by students, faculty, and technical staff. It is a traveling wave accelerator similar to the Mark III built at Stanford University, and consists of three 10 foot sections each individually powered by a klystron RF amplifier. The RF pulse length is 3.5 microseconds long and is pulsed at 120 hertz. The accelerator produces an average electron current of up to 10 microamps and accelerates electrons up to 100 MeV (Barnett, 1966). Figure 37 shows a schematic of the NPS Linear Accelerator, or linac, for short.

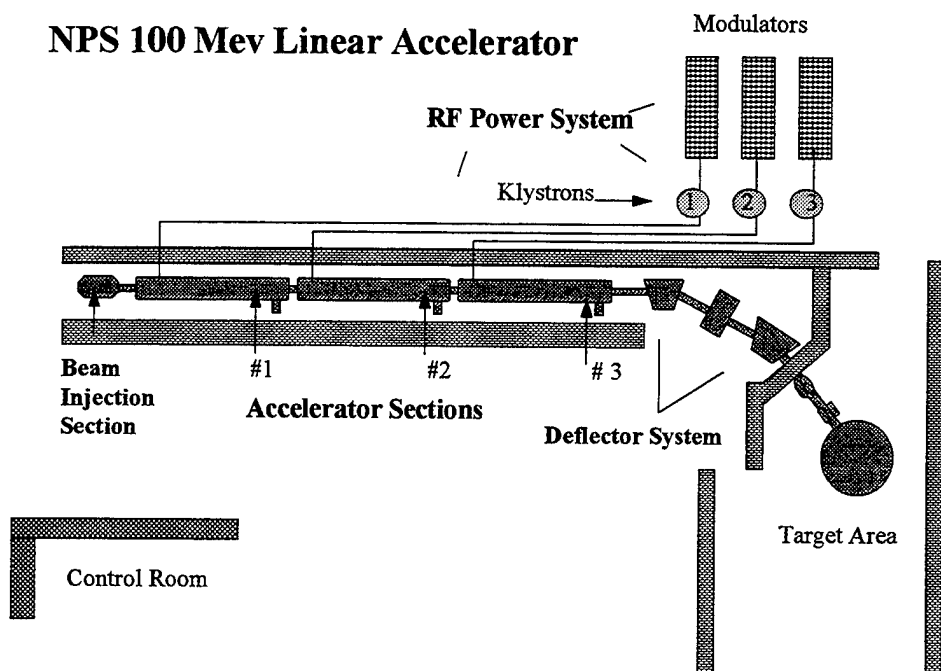


Figure 37. Schematic of the NPS Linear Accelerator.

This section of the thesis will describe the linac from the master oscillator all the way to the target area end-station and will discuss the theory and operation of the NPS linear electron

accelerator. During my research for this thesis, I spent almost a year learning about the NPS accelerator while it was being repaired following a catastrophic mechanical failure. The linear accelerator can be broken down into the following sections for purposes of this discussion--the RF power system, the injection system, the accelerator section, the deflection subsystem, and the target area.

## **B. THEORY OF ELECTRON LINEAR ACCELERATION**

In a traveling wave linear accelerator, particles experience a continuous accelerating force due to presence of an electric field in the direction of the beam. The wave velocity is equal to the desired velocity of the particle, so that the electron is accelerated if it is in phase with the appropriate half of the wave in the structure. There is a region of *phase stability* about the peak amplitude of the electric field wave where particles just ahead of the peak will be accelerated more slowly than the particles nearer to the peak, thereby drifting closer to the peak region (illustrated in Figure 38). Particles located immediately behind the peak will be accelerated towards the peak field. This results in a region where particles that start their journey in a phase stable region oscillate about the peak of the electric field phase and gain energy at the correct rate. As particle velocity become relativistic, these phase oscillations become less frequent and a maximum number of particles approach the crest of the electromagnetic wave resulting in a narrow spectrum of particle energy. (Barnett, 1966)

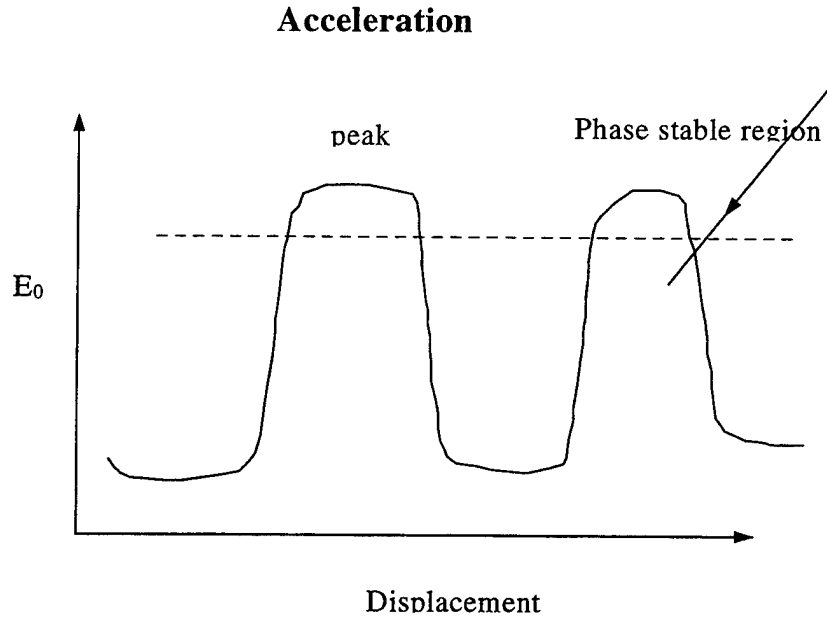


Figure 38. Diagram of phase stability in linac

### C. ELECTRON EMISSION

Electrons inside the metal cathode move about in a random manner due to thermal agitation. If an electron escapes from the surface, it leaves behind a net positive charge and the force retarding the electron emission is by Coulomb's law:

$$F = \frac{e^2}{4\pi\epsilon_0(r)^2} \quad (39)$$

where  $r$  is the distance from the electron to a positive image charge inside the metal surface. The electrostatic force goes to zero as  $r$  gets large, but acts to hold the electron as  $r$  remains small. Since the atomic spacing is of the order of an angstrom, the actual force on the electron matches the image distance starting at one angstrom. The work done in moving an electron from the surface is:

$$W = \int_0^r F dr . \quad (40)$$

The work required asymptotically reaches a constant value about 10 nm from the surface. This value represents a potential energy barrier that the electron kinetic energy must exceed and ranges from 1 to 6 eV at depending on the atomic structure of the material. This energy can be supplied by radiation, heat, external fields, or bombardment, causing electron photo-emission, thermionic emission, field emission, or secondary emission respectively. (Seymore, 1981)

#### D. ELECTRON MOTION IN A UNIFORM ELECTRIC FIELD

Electrons escape from the surface of the cathode, which is shaped like a depressed spherical section for uniform emission characteristics, and are accelerated towards the anode. The electrodes are held in a vacuum to avoid collisions with air molecules. The electric field, neglecting edge fringing, is uniform away from the cathode. The force  $F_z$  the electron sees is:

$$F_z = -eE_z = e \frac{dV}{dz} \quad (41)$$

Moving between two points, a and b, the work done on the electron is:

$$W_{ab} = \int_a^b F_z dz = e \int_a^b dV = e(V_b - V_a) \quad (42)$$

where  $V_a$  and  $V_b$  are the potentials found at each point. The force can be expressed as a change in momentum such that:

$$F_z = \frac{d}{dt}mv = m \frac{dv}{dt} + v \frac{dm}{dt} \quad (43)$$

If the electron velocity,  $v$ , remains below 0.2  $c$ , we can neglect the effects of relativistic mass increase and:

$$W_{ab} = \int_a^b F_z dz \cong \int_a^b m \frac{dv}{dt} dz = \int_a^b m v dv = \frac{1}{2} m (v_b^2 - v_a^2). \quad (44)$$

Equating formulas yields:

$$W_{ab} = e(V_b - V_a) = \frac{1}{2}m(v_b^2 - v_a^2). \quad (45)$$

Which indicates that the electron kinetic energy is a function of the energy gained from the electric field. Using the simplest model, the initial velocity is zero at the cathode and the velocity is a maximum at the anode because the voltage rises linearly between the two electrodes. The acceleration of an electron from rest is uniform and rises linearly with time:

$$\frac{dv}{dt} = A \frac{eV_{anode}}{m} \quad (46)$$

where A represents the slope of the increasing velocity versus time line. The average velocity is one half the final velocity and the transit time from cathode to anode is given by:

$$\tau = \frac{2A}{v_{anode}} = \sqrt{\frac{2m}{eV_{anode}}} \quad (47)$$

The mass of the electron is small, so little time is required for the electron to accelerate to relativistic velocities and gain mass energy. (Seymore, 1981)

## E. RELATIVISTIC ELECTRON MASS INCREASE

The electrons thermionically emitted from the cathode of the gun are accelerated towards the positively charged anode by the 80 keV field inside the gun. These electrons are shaped by the remainder of the beam injection assembly for acceleration inside the resonant cavity sections of the linac. The electron quickly reaches ultra-relativistic speeds. Since mass and energy are related ( $E = mc^2$ ), and force is defined in relativistic dynamics

$$\begin{aligned}
F &= \frac{d}{dt}(mv) \\
dE &= Fdz = c^2 dm \\
c^2 dm &= \frac{d}{dt}(mv)dz = \left( m \frac{dv}{dt} + v \frac{dm}{dt} \right) dz \\
c^2 dm &= \left( m \frac{dv}{dz} \frac{dz}{dt} + v \frac{dm}{dz} \frac{dz}{dt} \right) dz \\
c^2 dm &= m v dv + v^2 dm \\
&\text{because } \frac{dz}{dt} = v \\
(c^2 - v^2) dm &= m v dv \\
\frac{1}{m} dm &= \frac{1}{c^2 - v^2} dv \\
\ln m &= \ln \left( \frac{1}{c^2 - v^2} \right) + \ln C \\
m &= \frac{1}{c^2 - v^2} C
\end{aligned} \tag{48}$$

Setting  $v=0$  and  $m=m_0$ , the electron rest mass,  $C = m_0 c$ . Therefore:

$$m = \frac{1}{\sqrt{1 - \frac{v^2}{c^2}}} m_0 \quad \text{and} \quad E = \frac{1}{\sqrt{1 - \frac{v^2}{c^2}}} m_0 c^2 = mc^2 \tag{49}$$

An applied voltage  $V$  will result in an increase in energy of

$$E - E_0 = eV \tag{50}$$

When the electron velocity approaches the speed of light,  $c$ :



$$\frac{v}{c} = \sqrt{1 - \frac{E_0^2}{E^2}} \quad (51)$$

and substituting  $E = E_0 + eV$ ,  $\frac{v}{c} = \sqrt{1 - \left( \frac{E_0}{E_0 + eV} \right)^2}$  (Seymore, 1981). (52)

Figure 39 shows the speed of an electron as a fraction of the speed of light as it increases in energy in terms of MeV. Figure 40 shows that the electrons in the NPS linac reach velocities greater than 0.9998 c!

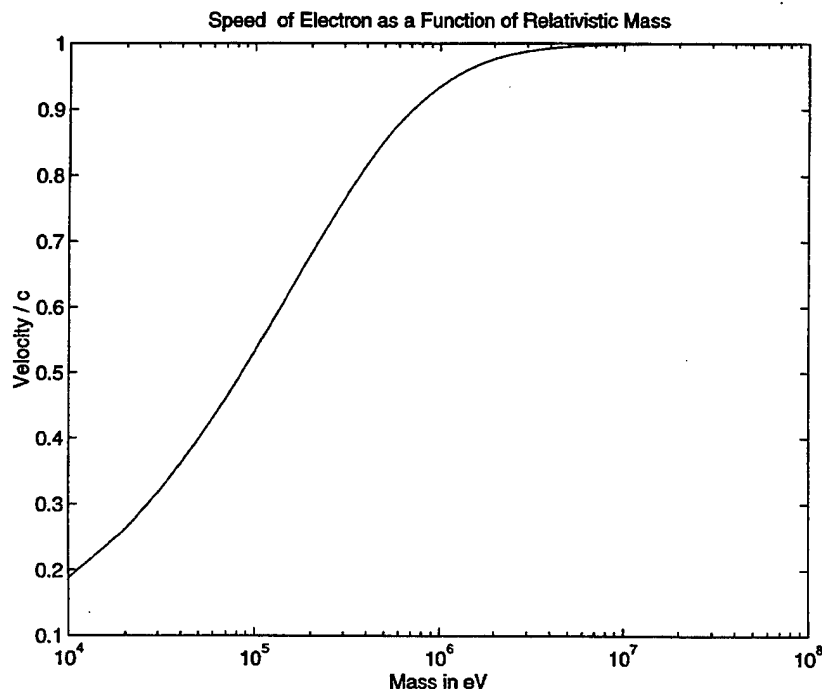


Figure 39. Speed of electrons in MeV.

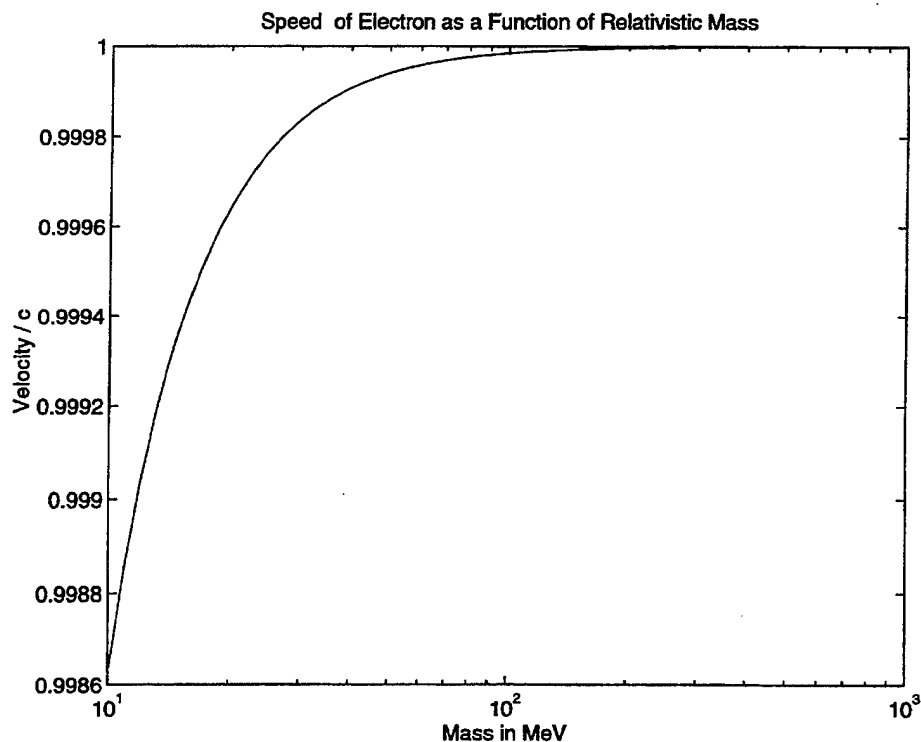


Figure 40. Speed of accelerated electrons at 100 MeV.

## F. ACCELERATING STRUCTURE

The electron linear accelerators built in the 1960s used disc-loaded waveguides consisting of metal discs with central irises periodically spaced along the otherwise cylindrical copper structure. These linacs were powered by pulsed RF energy to form either standing wave or traveling wave cavities. Electrons are accelerated by the cumulative effects of the electric field resonating inside the cavities and shielded as they pass between cavities. When the disk spacing is equal to half wave multiples of the RF guide, the disks have a large effect on the electric field. As the iris size becomes smaller, the effect increases. The dimensions are chosen to give the largest axial field strength available for a given input. See Figure 41 for a photograph of the cavity structure. This section will discuss the main design parameters for an electron linear accelerator. (Barnett, 1966)

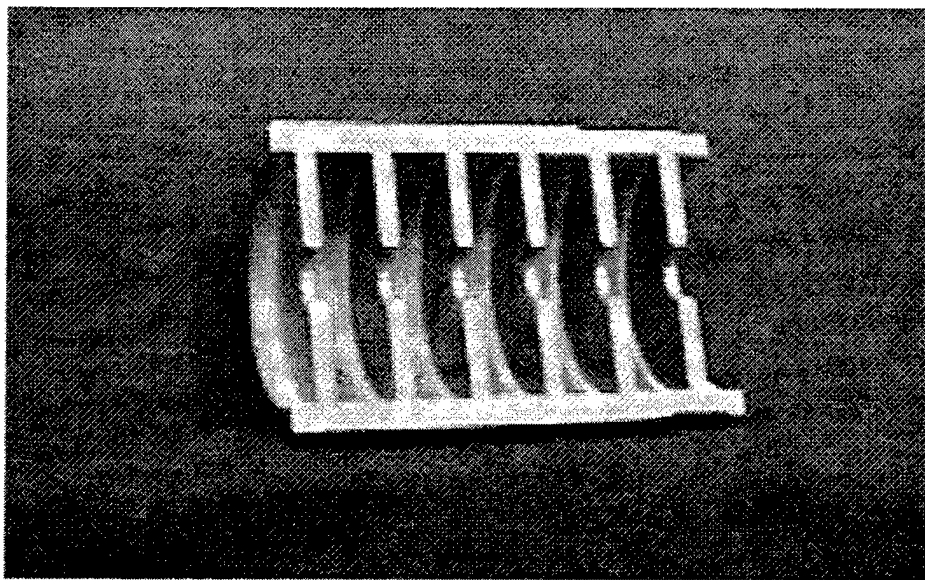


Figure 41. Photograph of a cutaway section of the accelerating cavity.

The *shunt impedance* is a measure of performance for a linac:  $r_0 = E_{0z}^2 / (dP/dz)$ . It is given as shunt impedance per unit length and is defined as the ratio of the amplitude squared of the axial electric field to the RF power dissipated per unit length. A high value is preferred which indicates that there are space harmonics present in the electric field that travel near the electron velocity. There are a large number of higher order electric field modes present in the cavities, but these harmonics tend to merely perturb the motion of the electrons and not produce useful acceleration.

The  $Q$  of an RF cavity is a measure of performance as a resonator. It is defined as the ratio of the energy stored in the cavity to the energy lost due to RF dissipation per radian of the RF cycle.  $Q$  can be expressed as ratio of the RF angular frequency times the energy stored per unit length to the RF power loss per unit length:  $Q = -\omega w / (dP/dz)$ . The ratio of shunt impedance to  $Q$  is therefore a measure of the square of the electric field in the structure in terms of the energy stored per unit length.

The *group velocity*,  $v_g$ , is the velocity at which RF energy flows through the accelerator and is dependent on the ratio of the diameter of the iris to the diameter of the accelerator cavity. The group velocity determines the filling time of a cavity with RF energy, and here a high  $v_g$  is

preferred. A low  $v_g$  would be better for two other factors: the power flowing into a cavity is equal to the product of the group velocity and the angular frequency, and the shunt impedance and Q of a cavity are inversely proportional to the  $v_g$ . The selection of a group velocity must be a compromise between maximizing accelerating fields for a given power and minimizing the time for the RF pulse.

The *frequency* for a given accelerator determines several important parameters-- the square of the shunt impedance is proportional to the frequency:  $r_0 \propto \omega^2$ , the ideal iris diameter is proportional to the inverse of the frequency, the filling time of a cavity varies as  $\omega^{-2/3}$ , and the dimensional tolerances for the physical cavities are proportional to  $\sqrt{\omega}$ .

The *operating mode* is defined as the ratio of  $2\pi$  to the number of disks per guide wavelength :  $\Phi_0 = 2\pi / n$ . Since most accelerators are designed for  $n=2,3$  or 4, the operating modes are either  $\pi$ ,  $\frac{2}{3}\pi$ , or  $\frac{\pi}{2}$ .

The *attenuation constant* is defined as the one-way RF attenuation in an accelerator of length  $l$  in nepers. (Lapostolle, 1970)

## G. THE RF POWER SYSTEM

The master oscillator is a resonant crystal oscillator that produces a very sharp pulse that becomes the mother signal for pulsing the klystron amplifiers. The electronic signals from the control panel trigger generator ensure that the electron gun pulse is synchronized with the klystron modulators to orchestrate the generation of the electron beam. Each klystron modulator receives a signal from the trigger generator and supplies a 42 kV charging pulse to the pulse line (the circuit that amplifies the drive power), which discharges a 250 kV voltage pulse to the its klystron. All of the electronics are controlled from the control section on the Linac (see Figure 42).

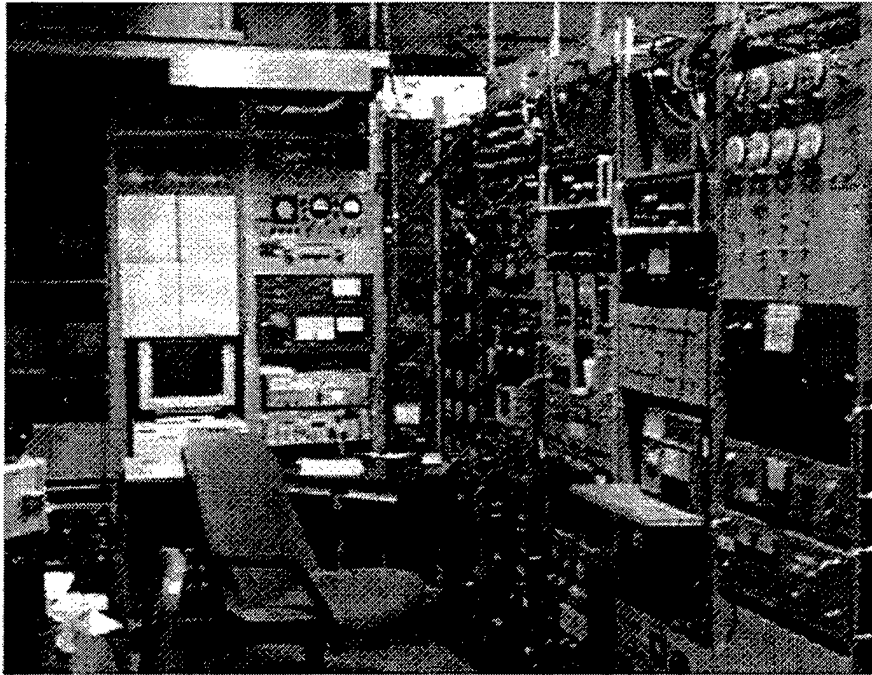


Figure 42. The Linac Control Room.

The pulse generator uses commercial three-phase 208-volt AC power which leads into a set of six variacs. This voltage is stepped up by a transformer in a delta-Y connection and fed into a three-phase full wave rectifier network. This charges the pulse-forming network (the pulse line), which is a parallel connection of 15 capacitors and inductors. The trigger generator sends a signal to the pulse-forming network to discharge into the pulse transformer through a thyatron switch mechanism. The pulse transformer steps up the discharge voltage to 250 kV which is then supplied to the cathode. The transformer is immersed in a dielectric oil bath, known as the klystron tank, to prevent high voltage induced ionization of the air (electrical breakdown). (Barnett, 1966)

#### **H. ELECTRON BEAM INJECTION**

The electron gun is controlled by an 8-kV and a 16-kV power supply. The 8 kV power supply provides grid power to the gun assembly while the 16 kV supply is applied to a 5:1 step-up pulse transformer leading to the cathode. The larger supply is triggered by a thyatron microwave tube. The cathode circuit has a low impedance, which would tend to lengthen the rise and fall times of the trigger pulse. This is overcome by using a bias resistor to keep the grid

circuit negative with respect to the cathode. By quickly pulsing the voltage on the grid to 3.5 kV positive relative to the cathode, a sharp trigger pulse is formed on the cathode with steep rise and fall times. An average current meter indicates the current leaving the gun.

The beam injection system is the first physical section of the accelerator. The klystrons produce the electromagnetic traveling waves, which are sent to the accelerator through waveguides and injected into each of the three 10 foot sections at the proper time interval. The timing of the electron injection is quite important and occurs during each klystron pulse. The RF energy from the klystron requires almost one microsecond to stabilize within the each accelerator cavity. Following this transient period there is a 2.5 microsecond period of the fully developed  $TM_{010}$  mode within the accelerator. This is the window for electron injection. Figure 43 shows the beam injection system of the NPS linear accelerator. (Barnett, 1966)

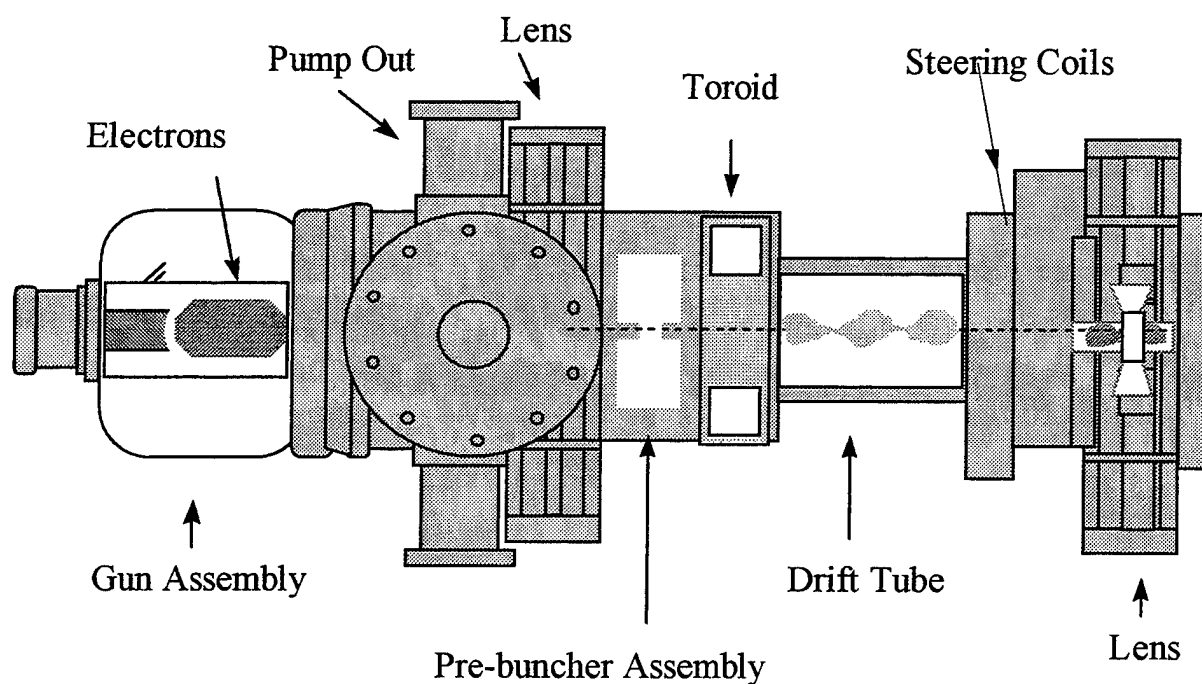


Figure 43. The Beam Injection Section

The electron gun provides a well formed pulse of electrons with a short build up and decay period and a relatively constant amplitude during the pulse. This provides a group of electrons that have a predictable and uniform energy spectrum. The 80 keV electron gun produces electrons traveling at about 0.5 c, but the RF wave in the accelerator travels at the

travels at the speed of light. The optimum electric field strength to capture electrons can be found by defining a capture parameter equal to twice the wavelength of the RF field times the electric field strength expressed in MeV/cm:  $\alpha_{opt} = 2E_0\lambda$ . The optimum value for the capture parameter is:  $\alpha_{opt} \cong 2\pi\sqrt{\frac{1-\beta}{1+\beta}} = 3.6$  where  $\beta = 0.5$  is the velocity of the electrons injected. This gives an optimum electric field strength of 0.17 MV/cm which equates to a power input of 13 MW. The beam of electrons from the gun should be aimed directly into the first magnetic lens, which in turn is aligned with the pre-buncher, toroid magnet, and second magnetic lens assembly. These elements comprise the initial section of the linac that injects well defined batches of electrons into the first stage cavity. Each magnetic lens is designed to aim the beam correctly. The radial component of the magnetic lenses cause electrons away from the center of the beam axis to rotate around the axis. The rotating electrons interact with the axial field component and experience a force directing them back towards the axis. Following the first magnetic lens is the pre-buncher. The electric field in the pre-buncher changes as each pulse of electrons passes through. The early electrons transfer energy to the field which slows them down and tends to increase the electron density in the pulse. Lower energy electrons will be accelerated. The toroid is a pulse transformer with the electron beam as its primary turn. The beam induces current pulses on the secondary turns, which is measured to indicate the pulsed beam current leaving the gun. The drift space allows the velocity differential to spatially bunch the electrons prior to entry into the first 10 foot accelerator section. There is a set of steering coils located at the end of each drift tube known as Hemholtz coils. These compensate for small alignment errors in the accelerator sections and for the perturbations introduced to the beam by the earth's magnetic field. The final component of the injection system is the second magnetic lens which focuses the electrons into the first RF coupler. (Barnett, 1966)

## I. THE RESONANT CAVITY

The linac is primarily a circular pipe constructed to confine and propagate the electromagnetic waves produced by the klystron that are injected from the rectangular waveguides. It is both a waveguide and an accelerating structure. In free space these RF waves will not propagate particles because the components of their electric and magnetic fields are

perpendicular to the direction of propagation. The copper conducting pipe has resonant cavities that are excited by the RF energy and produce an electric field in the direction of propagation. Figure 44 shows the transverse electromagnetic mode that the NPS linac uses to longitudinally accelerate electrons. The charges on the electrons in the beam tend to separate them from each other so the magnetic field of the toroid opposes their outward expansion. A round waveguide will have the following relationship between the group velocity and phase velocity:  $c = \sqrt{v_g v_p}$ .

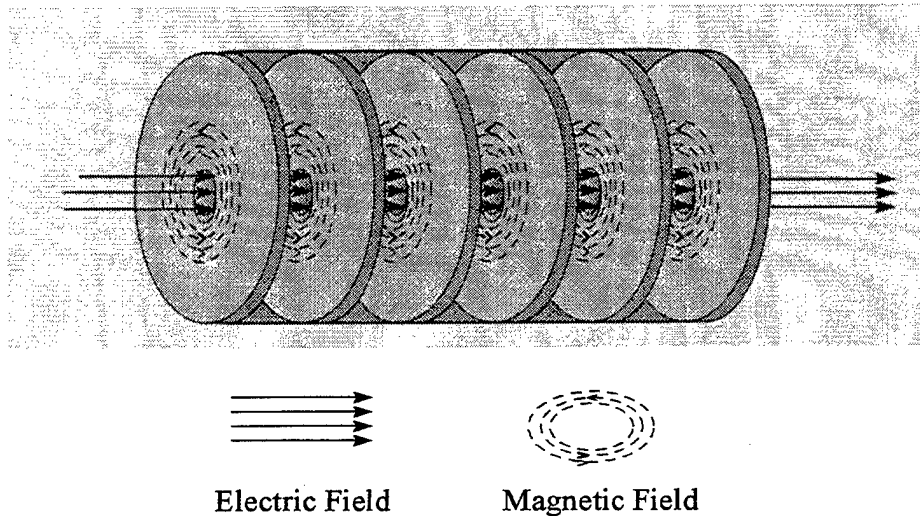


Figure 44. The Transverse Electromagnetic Mode 010.

Information travels at a maximum velocity equal to the speed of light in a vacuum, and so the phase velocity must be equal to or greater than then  $c$ . But we intend to accelerate the electrons to the phase velocity! The fix is to alter the electric and magnetic field inside the waveguide. If the pipe is loaded with metal conducting annular disks, then the group velocity is proportional to the ratio of the annular diameter ( $a$ ) to the pipe diameter ( $b$ ) to the forth power:  $v_g \propto (a/b)^4$ . The phase velocity is proportional to the diameter of the pipe. The annular disks provide openings for the electron beam and the RF waves to be transported from one cavity to the next throughout the linac. The dimensions of the opening determine the degree to which the TM010 mode couples with adjacent cavities and provides for the phase shift between cavities that gives an overall phase velocity equal to the speed of light over the length of the accelerator. The NPS linac uses a waveguide with a pipe diameter of 3.247 inches and an annular opening of



0.8225 inches. This gives a group velocity of  $0.01\ c$  and a phase velocity of  $c$ , the desired velocity of our electrons. The spacing of the disks was chosen to be one quarter of the RF wavelength and is equal to 1.0335 inches. The thickness of the disks was chosen to be 0.23 inches for rigidity. Tolerances in the manufacture process are very tight, and the disk dimensions must be of the order of 0.0002 inches. Figure 40 showed a cut-away view of an actual cavity from an accelerator cavity prototype. The volume inside each resonant section is critical. During manufacture, volume is carefully tested and tuning dimples are pressed into the sides of the cavities to optimize the resonant properties of each space. (Barnett, 1966)

Temperature control is important due to the heating of the waveguide by the RF wave attenuation. Cooling is provided by a water jacket around the waveguide that is circulated during operation. The transverse magnetic oscillation used in linear electron accelerator cavities is the  $TM_{010}$  mode. The dimensions of the cavity must be designed for the particular RF wavelength chosen.

The entire linear accelerator accelerating structure is enclosed in a concrete block chamber to provide radiation shielding. The housing chamber provides mounting for the klystron waveguides and electronic wiring necessary for monitoring the components of the system. Figure 45 shows a photograph of the inside of the housing showing the cooling jacket around the accelerating structure. Lead bricks can be observed lining the chamber walls at critical areas to increase the radiation shielding.

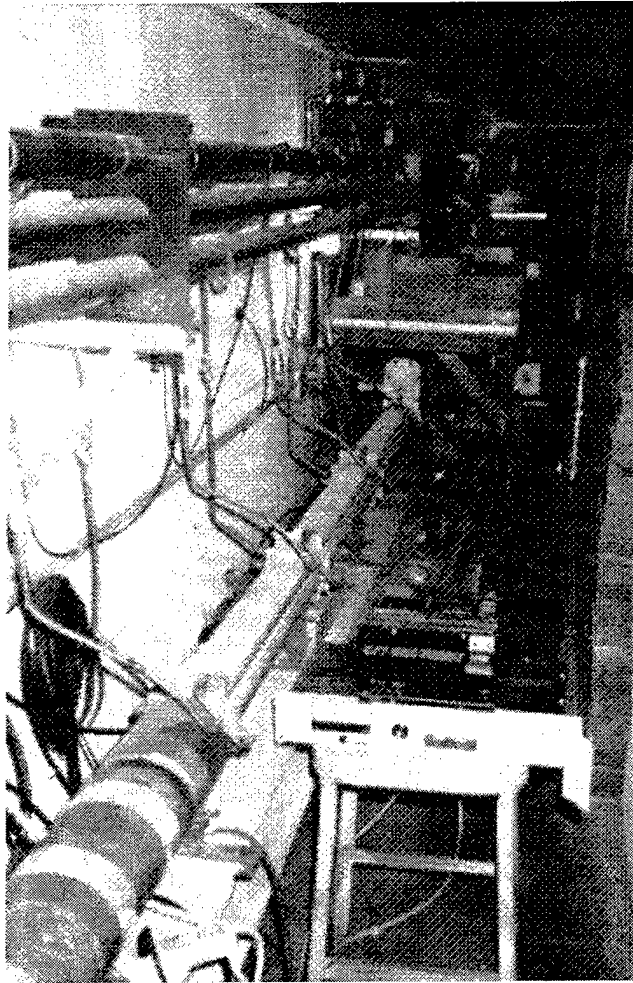


Figure 45. The inside of the housing containing the accelerating structure.

## J. THE KLYSTRON

The heart of the radio frequency power system is the klystron. Its development made possible electron accelerators and marks an important start to high energy physics research. Electrons are emitted thermionically from a cathode and enter a buncher cavity modulated by an alternating voltage supplied by the pulse transformer. The klystron uses velocity modulation to bunch electrons as they pass through a series of four more resonant cavities. The final cavity contains an RF output that harvests the sharply pulsed energy of the velocity modulated electron bunches. The intense RF energy is transported from the klystrons to the accelerator sections using rectangular metal waveguides. The collector at the top of the klystron catches the

collector. Shielding is also required due to the formation of Bremsstrahlung radiation. There is a large magnetic field around the klystrons due mainly to large electromagnets that provide focusing for the electromagnetic energy. Figure 46 shows the klystron amplifiers used in the NPS linac. They are velocity modulation amplifiers that produce high power pulses of electron bunches which produce the high amplitude output signal.

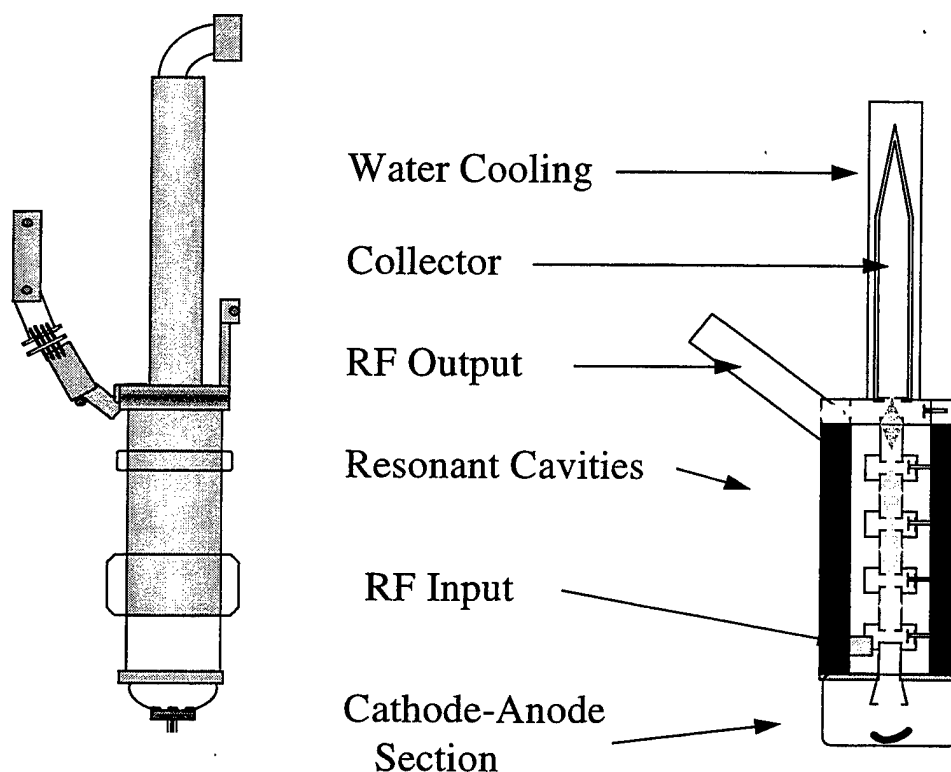


Figure 46. The klystron RF amplifier.

The klystrons are driven by a tunable magnetron oscillator that operates at 2.856 Ghz. The driver output is a waveguide that leads to a directional coupler that directs the excitation pulse simultaneously to each klystron. The power level to each klystron is controlled by variable attenuators located inside each feed line. The timing of the drive pulse must be delayed prior to klystron #2 and #3 by using a variable phase shifter, which is adjustable from the control room. This ensures that the RF traveling waves filling these accelerator sections are timed to coincide with the arrival of electrons from the previous section departure end drift tube. The energy from

from each section is dumped into an attenuator prior to the drift tube, thus eliminating the need to couple RF waves between each section in the accelerating structure. (Barnett, 1966)

## K. THE DEFLECTION SYSTEM

The final component of the accelerator section is a second toroid pulse transformer. This permits the operator to determine the peak current exiting the accelerator section. The *collimator* is the first subassembly in the deflection system of the linac. The first *deflection magnet* bends the beam and separates it into a spectrum of velocity energies. The *energy defining slits* allow only a narrow band of electron energies through. The second deflection magnet focuses the beam towards the target chamber. The deflection section of the linac is surrounded by two feet of concrete to attenuate radiation generated by the lateral acceleration of electrons in the beam due to the deflection magnets and due to Bremsstrahlung (stopping radiation) when electrons impact the walls of the linac and the target chamber. See Figure 47 for a photograph of the quadrapole magnet at the end of the deflection section and Figure 48 for a schematic of the overall deflection system of the NPS linac.

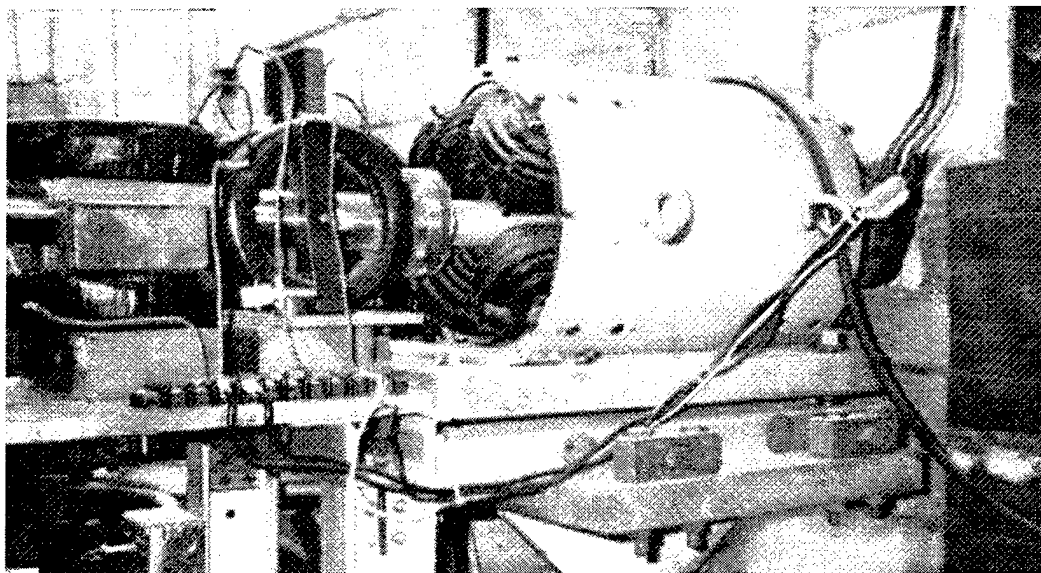


Figure 47. The quadrapole magnet assembly

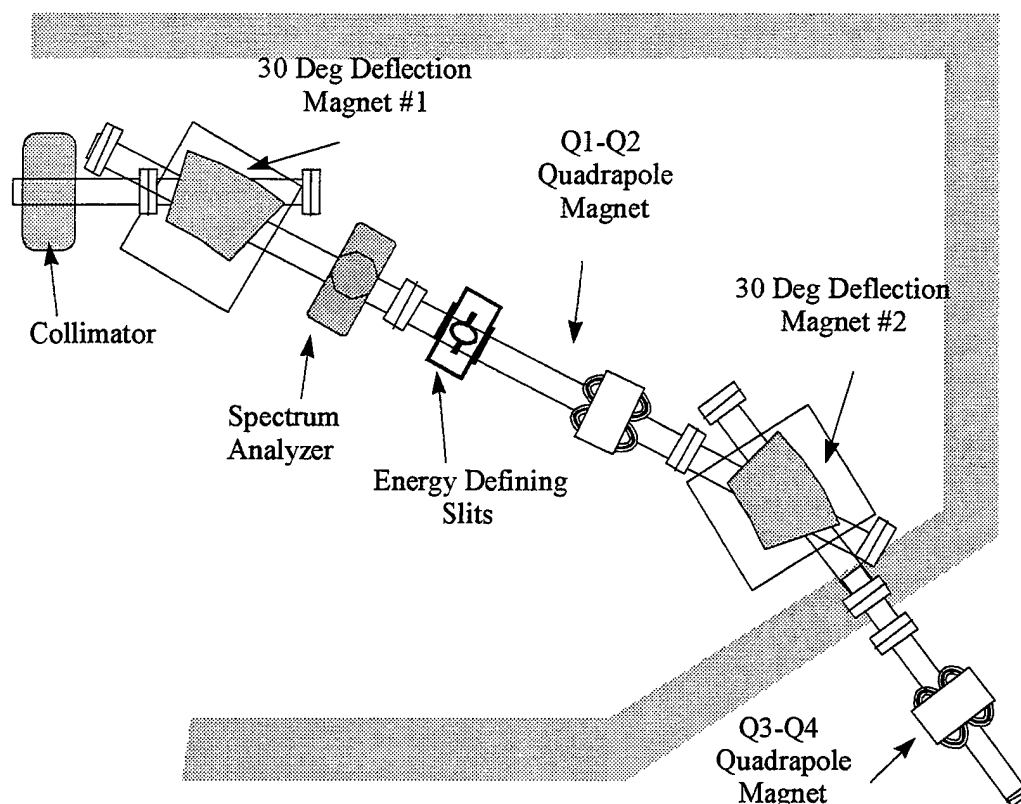


Figure 48. The Deflection System of the NPS linac.

## L. THE END STATION TARGET CHAMBER

The final section of the linac is the target chamber. The entire internal part of the linac must remain under a tight vacuum in order to have an electron beam. This is accomplished with several vacuum pumps located at each section of the accelerating structure and at the end station. The end station was mounted on a 5 inch gun turret to allow rotation of the assembly and reasonable angle determination for the various exit ports. Due to the radiation produced by the electron interactions in the target chamber, the entire subassembly is surrounded by concrete and cinderblock walls. During the thesis experiment, the target chamber was controlled remotely using DC motors and digital cameras. The polycapillary lens mount has adjustments that were made from the control room. Digital cameras are also used to monitor conditions and to record data for later analysis. Figure 49 shows the busy layout of the end station during the thesis

experiments. The digital cameras used to monitor conditions are visible in the foreground and the lasers used for alignment in the background.

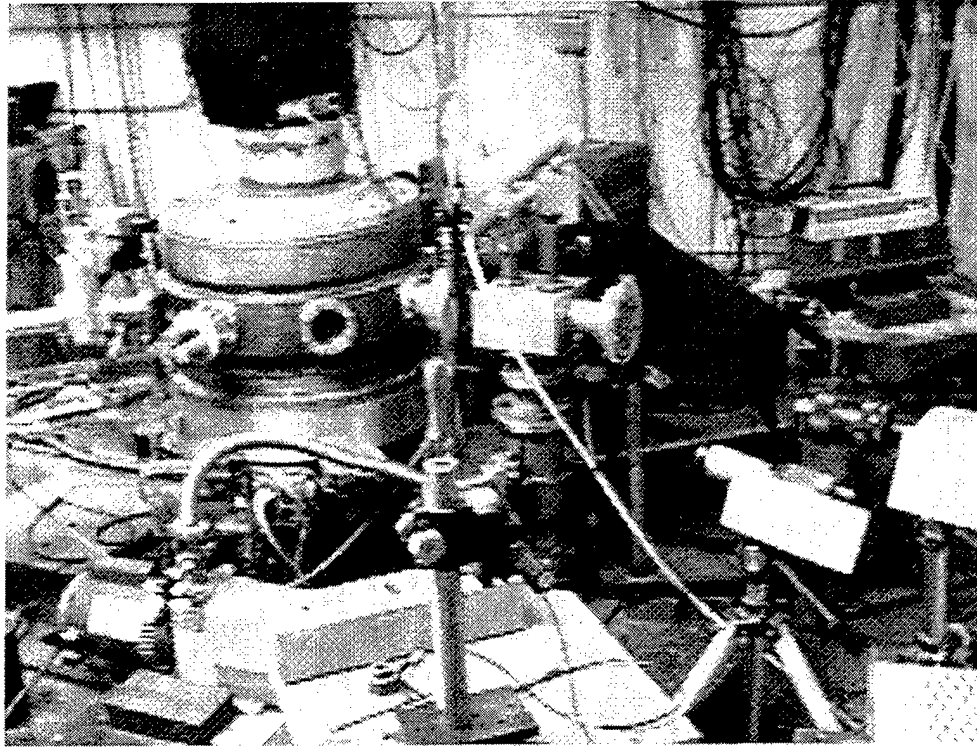


Figure 49. The NPS linac target chamber.

The final element in the linac is the beam dump, which is the termination point for the electrons and the radiation generated during experimentation.

## LIST OF REFERENCES

- Barnett, M. T., and Cunneen, W. J., *Design and Performance of the Electron Linear Accelerator at the U. S. Naval Postgraduate School*, Thesis, United States Naval Postgraduate School, May 1966.
- Dammel, R., *Diazonaphthoquinone-based Resists*, SPIE Optical Engineering Press, Vol. TT 11, 1993.
- Gunther, R. D., *Modern Optics*, John Wiley and Sons, 1990.
- Hollinger, S. J., *A Six-Pack for the Mac*, ESD: THE Electronic System Design Magazine, June 1989.
- Lapostolle, P. M., Septier, A. L., *Linear Accelerators*, John Wiley and Sons, 1970.
- Maruyama, X. K., Neighbors, J. R., Burskirk, F. R., Snyder, D. D., Vujaklija, M., Bruce, R. G., *Observation of Microwave Cerenkov as a Diffraction Pattern*, Journal of Applied Physics, Vol 60, 1986.
- O'Grady, A. J., *Cherenkov Radiation, Transition Radiation and Diffraction Transition Radiation from Periodic Bunches for a Finite Beam Path in Air*, Thesis, United States Naval Postgraduate School, June 1986.
- Piestrup, M. A., Moran, M. J., Berman, B. L., Pianetta, P., Seligson, D., *Transition Radiation as an X-Ray Source for Lithography*, Electron-Beam, X-Ray, and Ion-Beam techniques for Submicrometer Lithographies VI, Proceedings of SPIE-The International Society for Optical Engineering, Vol 773, March 1987.
- Piestrup, M. A., Boyers, D. G., Pincus, C. I., Qiang Li, Hallewell, G. D., Moran, M. J., Skopik, D. M., Silzer, R. M., Maruyama, X. K., Snyder, D. D., Rothbart, G. B., *Observation of Soft X-Ray Spatial Coherence from Resonance Transition Radiation*, Physical Review A, Vol. 45, Number 2, 15 January 1992.
- Piestrup, M. A., Powell, M. W., Mrowka, S., Lombardo, L. W., Chase, M. B., Cremer, J. T., Maruyama, X. K., *A Single-Stepper Soft X-Ray Source for Step-and Scan Tools*, draft technical paper submitted to SPIE, March 1997.
- Klotzko, I. *Investigation of Glass Polycapillaries for Use in Proximity X-Ray Lithography*, Dissertation, University at Albany, State University of New York, 1996.
- Ruddell, R., *The Time has Come for X-Ray Lithography*, Electron-Beam, X-Ray, and Ion-Beam techniques for Submicrometer Lithographies IV, Proceedings of SPIE-The International Society for Optical Engineering, Vol 537, March 1985.

Seymour, J., *Electronic Devices and Components*, John Wiley and Sons, 1981.

Votruba, P. M., *Focusing X-Ray Transition Radiation with Cylindrical and Elliptical Optics*, Thesis, United States Naval Postgraduate School, December 1991.

Wartski, L., *Study on the Optical Transition Radiation Produced by 30 to 70 MeV Energy Electrons*, Dissertation, University of Paris-South, April 1976.

X-Ray Optical Systems, Inc. Homepage, *An Introduction to X-Ray Optical Systems, Inc. (XOS)*, [www.xos.com](http://www.xos.com), 1996.



## INITIAL DISTRIBUTION LIST

1. Defense Technical Information Center.....2  
 8725 John J. Kingman Rd. , STE 0944  
 Ft. Belvoir, Virginia 22060-6218
  
2. Dudley Knox Library.....2  
 Naval Postgraduate School  
 411 Dyer Rd.  
 Monterey, California 93943-5101
  
3. Dr. A. Atchley, Code Ph .....1  
 Department of Physics  
 Naval Postgraduate School  
 Monterey, California 93943-5101
  
4. Professor X. K. Maruyama, Code PhMx ..... 3  
 Department of Physics  
 Naval Postgraduate School  
 Monterey, California 93943-5101
  
5. LCDR Richard Harkins, Code PhHr .....1  
 Department of Physics  
 Naval Postgraduate School  
 Monterey, California, 93943-5101
  
6. Dr. M. A. Piestrup ..... 1  
 Adelphi Technology, Inc  
 532 Emerson Street  
 Palo Alto, California 94301
  
7. Mr. Don Snyder, Code Ph ..... 1  
 Department of Physics  
 Naval Postgraduate School  
 Monterey, California 93943-5101
  
8. Mr. Harold Rietdyk, Code Ph ..... 1  
 Department of Physics  
 Naval Postgraduate School  
 Monterey, California 93943-5101

9. Professor Bill Maier, Code PhMw ..... 1  
Department of Physics  
Naval Postgraduate School  
Monterey, California 93943-5101
10. CDR. Michael B. Chase, USN ..... 1  
600 Rockingham Road  
Orange Park, Florida 32073